NASA Contractor Report 3991

Transonic Airfoil Analysis and Design in Nonuniform Flow

Jen-Fu Chang and C. Edward Lan

GRANT NAG1-308
JUNE 1986

NASA Contractor Report 3991

Transonic Airfoil Analysis and Design in Nonuniform Flow

Jen-Fu Chang and C. Edward Lan
Flight Research Laboratory
The University of Kansas Center for Research, Inc.
Lawrence, Kansas

Prepared for
Langley Research Center
under Grant NAG1-308

National Aeronautics
and Space Administration

Scientific and Technical
Information Branch

1986

SUMMARY

A nonuniform transonic airfoil code is developed for applications in analysis, inverse design and direct optimization involving an airfoil immersed in propfan slipstream. Problems concerning the numerical stability, convergence, divergence and solution oscillations are discussed. The code is validated by comparing with some known results in incompressible flow. A parametric investigation indicates that the airfoil lift-drag ratio can be increased by decreasing the thickness ratio. A better performance can be achieved if the airfoil is located below the slipstream center. Airfoil characteristics designed by the inverse method and a direct optimization are compared. The airfoil designed with the method of direct optimization exhibits better characteristics and achieves a gain of 22 percent in lift-drag ratio with a reduction of 4 percent in thickness.

TABLE OF CONTENTS

TABLE OF CONTENTS, continued

LIST OF SYMBOLS

English Symbols	Definition
A_1	Constant in y-stretching function controlling the grid size near the airfoil
A_2	Constant in x-stretching function controlling the grid size near the interface
A_3	Constant in x-stretching function controlling the far-field grid size.
a	Speed of sound, or Coefficient of coordinate transformation in airfoil region. See Equation (21).
a_j	Fourier coefficients in Equation (39)
b	Coefficient in coordinate transformation. See Equation (21).
c_ℓ	Sectional lift coefficient
c_d	Sectional drag coefficient
c_m	Sectional pitching moment coefficient relative to the quarter chord
C_p	Pressure coefficient
D	Total derivative, or Drag
F	Rotation function, or Objective function
f	Transformation in the x direction
G	Constraint function
g	Transformation in the y direction
ILE	x-direction index at the leading edge
ITE	x-direction index at the trailing edge
IMAX	x-direction index in the positive far field

LIST OF SYMBOLS, continued

English Symbol	Definition
JMAX	y-direction index in the positive far field
JB	Index for solid boundary points
$\vec{k}$	Unit vector in the z-direction
L	Lift
L/D	Lift-to-drag ratio
M	Mach number
N	Number of interpolation points
NIC	Number of constraints
p	Pressure
P	Some quantity
$\vec{q}$	Velocity vector
R_p	Radius of the propfan slipstream
THTE	Allowable trailing edge thickness
t	Time
u	Velocity component in the x direction
v	Velocity component in the y direction
x	Axis pointing downstream
x_1	x-coordinate after which airfoil shape is allowed to change
x_4	x-coordinate where two coordinate transformations meet
y	Axis normal to the x axis and pointing upwards, or Airfoil ordinate

LIST OF SYMBOLS, continued

Greek Symbols	Definition
α	Angle of attack
β	Prandtl-Glauert compressibility factor
γ	Ratio of specific heats
Γ	Circulation
ξ	Transformed coordinate in the x direction
ξ_4	ξ coordinate where two coordinate transformations meet
η	Transformed coordinate in the y direction
θ	Polar angle
ρ	Density
ρ_o	Reference density
ϕ	Disturbance potential
Φ	Velocity function
ψ	Stream function
ω	Vorticity
∇	Del operator
Δx	Spacing in the x coordinate
Δy	Spacing in the y coordinate
$\Delta\tau$	Spacing in the transformed x coordinate
$\Delta\Phi_{max}$	Maximum difference among $\Delta\Phi$ relative to previous iteration

LIST OF SYMBOLS, continued

Superscripts and Subscripts	Definition
$\rightarrow$	Vector
$-$	Nondimensional quantity
o	Stagnation quantity, or Quantity on the axis, or Reference quantity
∞	Freestream quantity
$\| \|$	Absolute value
b	Boundary quantity
ℓ	Lower limit
n	Normal direction
ref	Reference quantity
s	Streamline direction
sw	Swirl quantity
te	Trailing edge
u	Upper limit

LIST OF SYMBOLS, continued

Abbreviations	Definition
NASA	National Aeronautics and Space Administration
ACEE	Aircraft Energy Efficiency program
QVLM	Quasi-Vortex Lattice Method (Ref. 24)
FLO28	A conservative transonic code (Ref. 28)
FLO22NM	A nonconservative transonic code with Nash-McDonald boundary layer method (Ref. 29)
CPU	Central Processing Unit
TRANDES	TRANsonic DESign (Ref. 42)
CONMIN	CONstrained MINimization (Ref. 35)

1. INTRODUCTION

Due to the energy crisis in 1973, NASA and industry began to search for ways to reduce aircraft fuel consumption and established the Aircraft Energy Efficiency (ACEE) program. It was found that turboprop engines have the potential to significantly reduce fuel consumption for a given mission relative to advanced turbofans used today by extending their high propulsive efficiency to about Mach 0.8. To do this, Hamilton Standard proposed the Propfan (Ref. 1) concept, using thin, short, multi-swept blades and area-ruled spinner and nacelle to reduce the wave drag.

Under the sponsorship of ACEE, NASA and industry (Refs. 2-4) performed extensive studies and concluded that in the absence of excessive aerodynamic interference, propfan propulsion systems are 18 percent more efficient in the net thrust specific fuel consumption than high by-pass-ratio turbofans at Mach 0.8. They are even better for lower Mach numbers. Such potential benefit led to the establishment of the NASA high-speed turboprop program (Ref. 5). Windtunnel tests (Refs. 6-15) were conducted to provide data bases for verification of analytical and computational techniques, assessment of the magnitude of each factor, and installation aspects of the system. Welge and Crowder (Ref. 6) used an ejector-nacelle simulator to assess the magnitude of the aerodynamic interference of a simulated propeller stream on a 32°-swept supercritical wing-body. The interference drag amounts to an increase of ten drag counts (one drag count = .0001 of drag coefficient) for normal swirl angle. Up-inboard (positive) swirl generally was found to have less drag than up-outboard. These results were found to be independent of airplane lift coefficient or free-stream Mach number. For a 30°-swept supercritical wing-body, Boctor, et al. (Ref. 8) used a compressible panel method to perform the analysis and design. Test results for the configuration at a Mach number of 0.7 showed the potential for recovering up to 50% of the thrust lost due to swirl. However, at higher Mach numbers, the occurrence of shock wave and flow separation could offset the thrust recovery. Welge (Ref. 9) also used a compressible panel method to determine the flow field. He also studied the propfan integration for a DC-9 Super 80 with design Mach number of 0.8 based on the work in References 7 and 10. The propeller and forward nacelle are canted inboard 0.5 degree for alignment with local streamlines, and the region of the nacelle over the upper surface is aligned with the average surface streamline angle. The nacelle also had a 4.5° downtilt angle with respect to the propfan axis. He claimed that after offsetting unfavorable increment for weight, a 27 percent advantage in cruise specific fuel consumption over the current JT8D-209 was achieved. Smith and Levin (Refs. 11-12, 14) confirmed high drag for a nacelle installation in wind-tunnel testing. Inboard fillets and an outboard strake similar to that recommended in Reference 8 were tested and verified to reduce drag. Bartlett (Ref. 15) conducted wind-tunnel testing for a propfan installed on an upswept supercritical wing including overwing and underwing configurations. He found that the swirl is recoverable as thrust by the wing, and the propfan slipstream causes increase in wing lift.

From a theoretical point of view, when the free stream is nonuniform, the flow becomes rotational so that the potential flow equation is not valid. The main type of flow nonuniformity considered here arises from velocity variation inside the propfan slipstream and from different velocity magnitudes inside and outside the slipstream. When a wing section is immersed in the slipstream, its aerodynamic characteristics can be substantially different from those under a uniform flow condition with a free-stream velocity equal to an average value inside the slipstream or outside it. To predict correctly the aerodynamic characteristics, any theoretical method must be capable of properly accounting for the effect of this velocity nonuniformity.

Historically, Koning (Ref. 16) pioneered the formulation of the incompressible interaction problem involving a slipstream. Ferrari (Ref. 17) treated the compressible counterpart. A lifting surface theory for a circular jet was used by Rethorst (Ref. 18). Chow, et al. (Ref. 19), used the vorticity equation to solve the two-dimensional nonuniform incompressible flow by a finite difference method. Jameson (Ref. 20) combined the lifting line theory (for wing) and vortex sheets (for slipstream) to solve problems involving rectangular and elliptical slipstream. Ting, et al. (Ref. 21), used the lifting line theory and asymptotic expansion techniques to solve the interference of wings and multi-propellers. Using flow singularities, Shollenberger (Ref. 22) investigated wing/jet interaction without Mach number nonuniformity. Lan (Ref. 23) included compressibility effects by using the Quasi-Vortex-Lattice Method (QVLM, Ref. 24) plus two vortex sheets to represent the slipstream effects. Chin (Ref. 25) solved the inverse problem in two-dimensional nonuniform incompressible flow by using stream function formulation and the thin airfoil theory.

More recently, transonic effect on slipstream-wing interaction associated with propfan installation has received great attention. Various theoretical flow models and numerical schemes have been proposed. Rizk (Ref. 26) used two separate sets of transonic small-disturbance equations for inside and outside the slipstream and then imposed the interface conditions. He also included the assumption that the undisturbed velocity in the slipstream is nearly uniform. Samant, et al. (Ref. 27), applied a full potential code called FL028 (Ref. 28) based on a conservative finite volume approach to a wing-body configuration. The slipstream effect is simulated by the transpiration condition on the solid surface within the slipstream instead of the usual no-flow-through condition. Narain (Ref. 29) incorporated in the FL022NM code (Ref. 30) the slipstream effect by superimposing the rotational slipstream velocities into the coefficients of the steady nonconservative full potential equation by using either a rigid cylindrical semi-infinite slipstream model or a rigid converging one. The magnitude of these rotational velocities was calculated from propeller experimental data. Whitfield and Jameson (Ref. 31) used the three-dimensional, time-dependent Euler equation with force term (jump in total pressure) to simulate the propeller. They also incorporated a two-dimensional compressible turbulent inverse integral boundary layer code (Ref. 32) for the viscous displacement thickness effect. Shock can be captured.

Since supercritical wings have blunt noses, the small-disturbance assumption is not accurate near that critical region. Cylindrical modeling of the slipstream is not adequate for the lifting cases because the boundary will deform. The transpiration boundary condition, although accounting for the velocity increment of the propeller, causes absorption of energy from outside the cylindrical surface because the energy is conserved. The Euler code is theoretically ideal for the inviscid flow, but it requires comparatively long computer time. In addition, in all these theoretical methods no design of airfoils or wings has been considered.

In the present investigation, design of supercritical airfoils in transonic nonuniform flow will be emphasized. The formulation is to allow existing full-potential transonic codes to be modified for nonuniform flow through the introduction of a rotation function. The idea of using a rotation function in the full-potential equation was originated by Brown (Ref. 23) in solving a transonic nozzle flowfield. It is similar to the dual-potential approach adopted by Chaderjian and Steger (Ref. 34) to solve the transonic rotational flow. The effects of airfoil thickness, camber, swirl and airfoil location in and out of the slipstream will be examined. The design of airfoils will be done by both an inverse method and a direct optimization through an optimizer (Ref. 35).

2. THEORETICAL DEVELOPMENT

2.1 Equations for Two-Dimensional Nonuniform Flow

In the absence of viscosity, heat conduction and body forces, steady compressible flow is described by Euler's equation,

$$(\vec{q} \cdot \nabla)\vec{q} = -\frac{1}{\rho} \nabla p \tag{1}$$

and the continuity equation,

$$\begin{aligned} \nabla \cdot (\rho\vec{q}) &= \vec{q} \cdot \nabla\rho + \rho(\nabla \cdot \vec{q}) \\ &= \frac{D\rho}{Dt} + \rho(\nabla \cdot \vec{q}) = 0 \end{aligned} \tag{2}$$

where $\vec{q}$ is the velocity vector, ρ is the density, and p is the static pressure. If the two-dimensional stream function is defined as

$$\psi = \int \frac{\rho}{\rho_o} u dy \tag{3}$$

where ρ_o is the reference density, the Euler's equation along a streamline can be shown to be

$$\frac{Dp}{Dt} = -\frac{\rho}{2} \frac{D|\vec{q}|^2}{Dt} \tag{4}$$

Under isentropic assumption along a streamline, the substitution of $\frac{Dp}{Dt} = a^2 \frac{D\rho}{Dt}$ into Equation (4) gives

$$\frac{D\rho}{Dt} = -\frac{\rho}{2a^2} \frac{D|\vec{q}|^2}{Dt} \tag{5}$$

where a is the local speed of sound. For a two-dimensional flow, Equation (5) can be expressed in the following form:

$$(a^2 - u^2)\frac{\partial u}{\partial x} - uv\left(\frac{\partial v}{\partial x} + \frac{\partial u}{\partial y}\right) + (a^2 - v^2)\frac{\partial v}{\partial y} = 0 \qquad (6)$$

According to Brown (Ref. 33), nondimensionalizing Equation (6) with respect to the stagnation speed of sound gives

$$(\bar{a}^2 - \bar{u}^2)\frac{\partial \bar{u}}{\partial x} - \bar{u}\bar{v}\left(\frac{\partial \bar{v}}{\partial x} + \frac{\partial \bar{u}}{\partial y}\right) + (\bar{a}^2 - \bar{v}^2)\frac{\partial \bar{v}}{\partial y} = 0 \qquad (7)$$

which is seen to be of the same form as Equation (6). For simplicity, the bar notation will be neglected from now on. Define a velocity function Φ and a rotation function F such that

$$\begin{aligned} u &= \Phi_x + F \\ v &= \Phi_y \end{aligned} \qquad (8)$$

Substituting Equation (8) into Equation (7) gives

$$(a^2 - u^2)(\Phi_{xx} + F_x) - uv(2\Phi_{xy} + F_y) + (a^2 - v^2)\Phi_{yy} = 0$$

or

$$(a^2 - u^2)\Phi_{xx} - 2uv\Phi_{xy} + (a^2 - v^2)\Phi_{yy} = uv\,F_y - (a^2 - u^2)F_x \qquad (9)$$

where subscripts denote partial differentiation.

The two-dimensional vorticity vector $\vec{\omega}$ is given by

$$\vec{\omega} = \nabla \times \vec{q} = \vec{k}\left(\frac{\partial v}{\partial x} - \frac{\partial u}{\partial y}\right) \qquad (10)$$

where $\vec{k}$ is the unit vector in the z-direction. The magnitude of the vorticity vector, using Equation (8) is given by

$$\omega = |\vec{\omega}| = v_x - u_y = \Phi_{xy} - (\Phi_{xy} + F_y) = -F_y \qquad (11)$$

It follows that

$$F_y = u_y - v_x$$

$$= \left(1 - \frac{\gamma - 1}{2} M_o^{\,2}(\psi)\right) \frac{1}{\gamma u P_o(\psi)} \frac{\partial P_o}{\partial y} \tag{12}$$

where P_o is the stagnation pressure on a streamline, γ is the ratio of specific heats, and F, M_o and u are all referenced to the stagnation speed of sound (a_o) on a streamline. The F values are obtained by integrating Equation (12).

Local density is needed to calculate the stream function (see Equation 3). Along a streamline, density can be related to its stagnation quantity as

$$\rho = \rho_o(\psi)\left(1 - \frac{\gamma - 1}{2} M_{o_\infty}^{\;2}(\psi)\right)^{\frac{\gamma}{\gamma - 1}} \tag{13}$$

Since both $\rho_o(\psi)$ and $M_{o_\infty}(\psi)$ vary with streamline, they have to be calculated iteratively as follows:

(1) Assume the initial density distribution to be that of the undisturbed one.

(2) Calculate the stream function at a constant x according to Equation (3).

(3) Determine $\rho_o(\psi)$ and $M_{o_\infty}(\psi)$ as a function of ψ.

(4) Update ρ according to Equation (13).

(5) Check the convergence and decide if steps 2 to 5 should be repeated.

The iterative process will converge in several iterations. Note that the calculation of the rotation function F is updated according to Equation (12) as soon as the stream function is known at a given field point (step 5).

Along a streamline, the following form of energy equation for a perfect gas can be used:

$$\frac{1}{2} q^2 + \frac{a^2}{\gamma - 1} = \frac{1}{2} q_\infty^{\,2}(\psi) + \frac{a_\infty^{\,2}(\psi)}{\gamma - 1} = \frac{a_o^{\,2}(\psi)}{\gamma - 1} \tag{14}$$

If the entropy is assumed to be nearly constant along a streamline, i.e. only weak shocks are present, the pressure coefficient can be derived from Equation (14) as

$$C_p = \frac{p - p_\infty}{\frac{1}{2} \rho_{\infty_{ref}} q^2_{\infty_{ref}}}$$

$$= \frac{2}{\gamma M^2_{\infty_{ref}}} \left\{\left[1 + \frac{\gamma - 1}{2} M_\infty^{\,2}(\psi)\left(1 - \frac{|\vec{q}|^2}{|\vec{q}_\infty(\psi)|^2}\right)\right]^{\frac{\gamma}{\gamma-1}} - 1\right\} \tag{15}$$

2.2 Boundary Conditions for Two-Dimensional Flow

Assume $\rho_\infty u_\infty$ to be a function of y only in the free stream. Using the continuity equation for a two-dimensional flow,

$$\frac{\partial(\rho u)}{\partial x} + \frac{\partial(\rho v)}{\partial y} = 0 \tag{16}$$

it can be shown that $\rho_\infty v_\infty$ is a function of x only. Thus in the free stream, if v_∞ vanishes, then ρ_∞ may vary with y. On the other hand, if $v_\infty \neq 0$, then both ρ_∞ and v_∞ must be constant.

The free-stream rotation function is constructed from the difference in the undisturbed nonuniform velocity and the uniform part.

Since the free stream static pressure must be constant (Ref. 36), one of the following five parameters must be specified or assumed to be constant: stagnation pressure, temperature, stagnation temperature, density and stagnation density. For example, the experimental stagnation pressure is specified to simulate the power effect. Once one of the parameters is specified, the rest can be determined through the state equation and/or the isentropic compressible relations along a streamline.

According to References 37 and 38, the far-field boundary condition for Φ can be expressed as

$$\Phi = q_\infty(\psi)(x \cos\alpha + y \sin\alpha) + \frac{\Gamma}{2\pi} \tan^{-1}[\beta \tan(\alpha - \theta)] \qquad (17a)$$

where $q_\infty(\psi)$ is the free-stream velocity, α is the angle of attack, Γ is the circulation, β is the compressibility factor and θ is the corresponding polar angle. If the measured swirl angles (α_{sw}) are included, the following equation is used:

$$\Phi = q_\infty(\psi)(x \cos \alpha_{sw} + y \sin\alpha_{sw}) + \frac{\Gamma}{2\pi} \tan^{-1}[\beta \tan(\alpha_{sw} - \theta)] \qquad (17b)$$

Since Φ approaches infinity (Equation 17) at the far field, the far-field boundary condition is satisfied at midpoints of the two outermost transformed grid points.

The surface tangency condition is written as

$$\left(\frac{dy}{dx}\right)_b = \left(\frac{v}{u}\right)_b = \left(\frac{g\Phi_\eta}{F + f\Phi_\xi}\right)_b \qquad (18)$$

where b represents the boundary values. This equation, in combination with Equation (15), can be used for the inverse design:

$$\Phi_{x_b} = f_b \Phi_{\xi_b} = q_{\infty_{ref}} \{ \frac{1}{1 + (\frac{v_b}{u_b})^2} \cdot$$

$$\{1 - \frac{2}{(\gamma - 1) M_\infty^2(\psi)} [(1 + \frac{\gamma C_{p_b}}{2} M_\infty^2(\psi))^{\frac{\gamma-1}{\gamma}} - 1]\} \}^{\frac{1}{2}} - F \tag{19}$$

2.3 Coordinate Transformation

Following Carlson (Ref. 38), the flow field is divided into three regions as shown in Figure 1. The stretching is symmetrical about the origin and is given by

$$x = x_4 + A_2 \tan[\frac{\pi}{2} (\xi - \xi_4)] + A_3 \tan[\frac{\pi}{2} (\xi - \xi_4)^3] \tag{20}$$

in regions I and III and by

$$x = \xi(a + b\xi^2) \tag{21}$$

in region II. The constants a and b are determined by the requirements that

$$x = x_4 \text{ at } \xi = \xi_4 \tag{22a}$$

and

$$\frac{dx}{d\xi} = \frac{\pi A_2}{2} \text{ at } \xi = \xi_4 \tag{22b}$$

The constant A_2 controls the grid spacing in the vicinity of x_4, usually near the leading and trailing edges; while A_3 determines the physical location of the grid line adjacent to the grid edges.

In the y-direction, the stretching function is

$$y = A_1 \tan(\frac{\pi}{2} \eta) \tag{23}$$

where A_1 controls the grid size near the airfoil.

Notice that these stretchings map the infinite x,y plane

$$-\infty \leqslant x \leqslant \infty$$
$$-\infty \leqslant y \leqslant \infty \tag{24}$$

into the finite computation plane

$$-(1 + \xi_4) \leqslant \xi \leqslant (1 + \xi_4)$$
$$-1 \leqslant \eta \leqslant 1 \tag{25}$$

where ξ_4 determines the amount of the computational plane confined to the vicinity of the airfoil.

A typical grid system is shown in Figure 2.

Let P(x,y) be a function of x and y, and f and g be the transformations used in the y directions, respectively; i.e.,

$$f = \xi_x, \; g = \eta_y \tag{26}$$

where ξ and η are the transformed coordinates of x and y. The following relation can be derived:

$$P_x = P_\xi \xi_x = fP_\xi$$
$$P_y = P_\eta \eta_y = gP_\eta$$
$$P_{xx} = (fP_\xi)_\xi \xi_x = f(fP_\xi)_\xi$$
$$P_{xy} = (fP_\xi)_\eta \eta_y = fgP_{\xi\eta}$$
$$P_{yy} = (gP_\eta)_\eta \eta_y = g(gP_\eta)_\eta \tag{27}$$

Thus Equations (8) and (9) can be transformed into

$$(a^2 - u^2)f(f\Phi_\xi)_\xi - 2uvfg\Phi_{\xi\eta} + (a^2 - v^2)g(g\Phi_\eta)_\eta$$

$$= uvgF_\eta - (a^2 - u^2)fF_\xi \qquad (28)$$

$$u = F + f\Phi_\xi$$

$$v = g\Phi_\eta \qquad (29)$$

Since far-field boundary conditions of Φ are satisfied at the outermost half grid points instead of the edge points, using analytic expresions of f and g will make the computation of u and v very inaccurate, particularly in the far field. Therefore, the following first order approximation of f is used in regions I and III; and that of g is used for the outer half regions.

$$f = \frac{\partial\xi}{\partial x} \approx \frac{\Delta\xi}{\Delta x} \qquad (30)$$

$$g = \frac{\partial\eta}{\partial y} \approx \frac{\Delta\eta}{\Delta y} \qquad (31)$$

Similar problems occurred in calculating the stream function ψ. The stream function values are obtained by integrating from the far field in the lower half plane. In the far field, the y intervals are so large that any slight inaccuracy in u can cause large difference in ψ and thus the stagnation quantities on the airfoil streamline. Therefore, the reference point from which Equation (12) is integrated is shifted to the lower second grid point, instead of the exact far field.

Note that the value of stream function, and hence the rotation function, on the airfoil lower surface should be equal to that on the upper surface. However, because of numerical inaccuracy associated with integration between grid points and airfoil surface boundary points, their values may be different. In this case, their values are averaged for the purpose of identifying the dividing streamline.

The transformed Equation (28) is then reduced to a finite-difference form. To obtain the correct zone of dependence of Φ values in the supersonic region, the rotated difference scheme (Ref. 39) is used. Note that the latter is based on streamline coordinates s and n. Derivatives in streamline coordinates s,n and x,y coordinates are related as follows:

$$\begin{Bmatrix} P_s \\ P_n \\ P_{ss} \\ P_{sn} \\ P_{nn} \end{Bmatrix} = \begin{bmatrix} \frac{u}{q} & \frac{v}{q} & 0 & 0 & 0 \\ -\frac{v}{q} & \frac{u}{q} & 0 & 0 & 0 \\ 0 & 0 & \frac{u^2}{q^2} & \frac{2uv}{q^2} & \frac{v^2}{q^2} \\ 0 & 0 & -\frac{uv}{q^2} & \frac{u^2 - v^2}{q^2} & \frac{uv}{q^2} \\ 0 & 0 & \frac{v^2}{q^2} & -\frac{2uv}{q^2} & \frac{u^2}{q^2} \end{bmatrix} \begin{Bmatrix} P_x \\ P_y \\ P_{xx} \\ P_{xy} \\ P_{yy} \end{Bmatrix} \tag{32}$$

or, conversely,

$$\begin{Bmatrix} P_x \\ P_y \\ P_{xx} \\ P_{xy} \\ P_{yy} \end{Bmatrix} = \begin{bmatrix} \frac{u}{q} & -\frac{v}{q} & 0 & 0 & 0 \\ \frac{v}{q} & \frac{u}{q} & 0 & 0 & 0 \\ 0 & 0 & \frac{u^2}{q^2} & -\frac{2uv}{q^2} & \frac{v^2}{q^2} \\ 0 & 0 & \frac{uv}{q^2} & \frac{u^2 - v^2}{q^2} & -\frac{uv}{q^2} \\ 0 & 0 & \frac{v^2}{q^2} & \frac{2uv}{q^2} & \frac{u^2}{q^2} \end{bmatrix} \begin{Bmatrix} P_s \\ P_n \\ P_{ss} \\ P_{sn} \\ P_{nn} \end{Bmatrix} \qquad (33)$$

Now Equation (28) can be written as

$$(a^2 - q^2)\Phi_{ss} + a^2\Phi_{nn} = (q^2 - a^2)\,\frac{u}{q}\,F_s + a^2\,\frac{v}{q}\,F_n \qquad (34)$$

where

$$\Phi_{ss} = \frac{1}{q^2}\,[u^2f(f\Phi_\xi)_\xi + 2uvfg\Phi_{\xi\eta} + v^2g(g\Phi_\eta)_\eta]$$

$$\Phi_{nn} = \frac{1}{q^2}\,[v^2f(f\Phi_\xi)_\xi - 2uvfg\Phi_{\xi\eta} + u^2g(g\Phi_\eta)_\eta]$$

$$F_s = \frac{fu}{q}\,F_\xi + \frac{gv}{q}\,F_\eta$$

$$F_n = -\frac{fu}{q}\,F_\xi + \frac{gu}{q}\,F_\eta \qquad (35)$$

Equation (28) or (34) is seen to be quite similar to those used by Carlson (Refs. 38, and 40-42), except for the nonhomogeneous terms on the right side of the equation. Therefore, Carlson's transonic potential flow code, TRANDES, is modified to solve the present problem. Carlson's code has the following features:

(a) the coordinate system used was the Cartesian system.

(b) A rotated finite difference scheme was used.

(c) A damping term was added explicitly to the difference equations for numerical stability, instead of using Jameson's implicit damping formulation.

(d) Airfoil boundary conditions in both analysis and inverse design were satisfied by introducing dummy points inside the airfoil.

(e) The resulting finite-difference equations were of the tridiagonal type and were solved iteratively by column relaxation.

(f) The Nash-McDonald method is used for boundary layer calculation.

Main differences between the present formulation and Carlson's are as follows:

(a) A velocity function Φ is used in the present formulation, instead of Carlson's disturbance velocity potential. The latter approaches zero in the far field, but not the former (see Equation 17a). This behavior makes the far-field boundary conditions more difficult to satisfy in the present formulation. The Φ formulation is necessary in the present problem to result in the same form of the governing equation.

(b) The present equations are nondimensionalized with the stagnation speed of sound which varies from streamlines to streamlines. Therefore, the streamline with which a field point is associated must be identified in the relaxation solution.

2.4 Solution Procedures for Analysis and Inverse Design

The solution procedure for the transonic nonuniform flow consists of the following steps:

(1) Input options and parameters.

(2) Set up grid coordinates and transformations.

(3) Initiate or input variables.

(4) Input airfoil shape (analysis) or pressure distribution (design).

(5) Set up far-field values for Φ.

(6) Calculate stream function at the far field and set up interpolation coefficients for ρ_o, p_o, etc.

(7) Solve the flow field in front of the airfoil.

(8) Solve the flow field on the airfoil depending on analysis or design mode.

(9) Solve the wake region.

(10) Calculate circulation from Kutta conditions.

(11) Update the far-field boundary conditions.

(12) Periodically update the stream function, density, stagnation pressure and stagnation pressure gradient to obtain the new rotation function.

(13) In the design mode, periodically update the airfoil shape.

(14) In the analysis mode with viscous interaction option, periodically update the boundary layer thickness distribution.

(15) Repeat steps 7-14 until Φ converges or the number of iterations exceeds a limit.

(16) Calculate the last values of rotation funtion, shapes and boundary layer if applicable.

(17) Compute pressure distribution.

(18) Plot Mach plot.

(19) Compute airfoil characteristics.

(20) Plot pressure distribution.

(21) Halve the grid if applicable.

(22) Repeat steps 2-21 if applicable.

(23) In the design mode, subtract the boundary layer to obtain the actual airfoil shape.

2.5 Formulation for Direct Optimization

In a direct optimization to design an airfoil, the analysis method described above is coupled with an optimizer, CONMIN (Ref. 35). The design problem can be stated as follows:

Minimize

$$F = -\frac{c_\ell}{c_d} \tag{36}$$

Subject to

$$G_i \leq 0, \ i = 1, \ldots, NIC \tag{37}$$

where c_d is the sectional drag coefficient including wave drag and friction drag. G_i represents the constraints. Since the constraints work best when magnitudes of their gradients are of the same order of magnitude, a scale factor may be applied to constraints whose gradients are too small or too large.

The following constraint formulations have been used in the present optimization problem.

1. Lift constraint:

$$\begin{aligned} G_u &= \left(\frac{c_\ell}{c_{\ell(u)}} - 1\right) \times 10 \\ G_\ell &= \left(1 - \frac{c_\ell}{c_{\ell(\ell)}}\right) \times 10 \end{aligned} \tag{38}$$

where $c_{\ell(u)}$ and $c_{\ell(\ell)}$ are the prescribed upper and lower bounds of lift coefficient, respectively. This type of constraints is necessary because an exact numerical constraint on c_ℓ can not be achieved in a numerical optimization.

2. Trailing-edge closure constraint:

$$G_{te} = (Y_u - Y_\ell)_{te}/\mathrm{THTE} - 1.0 \tag{39}$$

where $Y_{u_{te}}$ and $Y_{\ell_{te}}$ are the nondimensional upper and lower surface coordinates at the trailing edge, respectively, and THTE is the allowable trailing edge thickness.

To reduce the number of design variables, airfoil coordinates are expressed in a Fourier cosine series, i.e.

$$y = \sum_{j=1}^{N} a_j \cos(j - 1)\,\theta \tag{40}$$

where y may be the upper or lower surface coordinates. The Fourier coefficients are given by

$$a_1 = \frac{1}{\pi} \int_0^{\pi} y \, d\theta$$

$$\approx \frac{1}{N} \sum_{K=1}^{N} y_K \tag{41a}$$

$$a_j = \frac{2}{\pi} \int_0^{\pi} y \cos(j - 1)\theta d\theta$$

$$\approx \frac{2}{N} \sum_{K=1}^{N} y_K \cos(j - 1)\ \theta_K \tag{41b}$$

$$\theta_k = (2k - 1)\pi/2N \tag{42a}$$

$$x = x_1 + 0.5 * (\frac{1}{2} - x_1)(1 - \cos\theta) \tag{42b}$$

where x_1 is the x-station after which the airfoil shape is to be modified. These Fourier coefficients are used as the design variables. Equation (40) is used only away from the nose region. This means that the nose region, within 5% say, remains unchanged during optimization. If the nose shape is to be changed, an expression different from Equation (40) should be used. The flow chart for the optimization is presented in Figure 3.

3. CONVERGENCE PROBLEMS AND SOLUTIONS

3.1 Grid Halving

Multigrid calculation is frequently used to accelerate the convergence. When the coarse grids are halved, medium grids are obtained with the number of grid points doubled. The starting values of Φ in the latter are normally obtained by interpolating the values of Φ in the coarse grids. In this process, the new starting Φ values in the far field may change so greatly from the values in the coarse grids as to cause divergence. A solution to this problem is to set the values next to the new far-field boundary to the old far-field values, i.e.

$$\begin{aligned} \Phi_{i,jmax-1(new)} &= \Phi_{i,jmax-1/2\,(old)} \\ \Phi_{i,2(new)} &= \Phi_{i,1+1/2\,(old)} \\ \Phi_{imax-1,j(new)} &= \Phi_{imax-1/2\,,j(old)} \\ \Phi_{2,j(new)} &= \Phi_{1+1/2\,,j(old)} \end{aligned} \tag{42}$$

where "new" indicates values in the medium grids and "old" means values in the coarse grids. Note that jmax is different in both grids. The new far-field Φ values (at the outermost half grid points) are calculated with Equation (17a).

Interpolation of old Φ values for the new grids is made only on the difference between the total Φ values and the undisturbed ones. The same process is used again when grids are further halved.

For Φ values across the Kutta-Joukowsky cut downstream of the trailing edge, the Φ values just below the x-axis are obtained by extrapolating those from the lower flow region.

3.2 Supersonic Damping Factor

Supersonic damping is needed for the stability of the relaxation solution involving supersonic flow region. In the present Φ-formulation, instead of the formulation with the disturbance velocity potential, a larger value of damping factor appears to be always needed. At the beginning of calculation in each grid system, a value of up to 5.0 is used in a transonic flow. During the iterative solution process, the damping factor will be increased by 0.1 if the cumulative $\Delta\Phi_{max}$ increases by a certain critical value, except that in the last grid calculation where an increment of 0.01 is used after 200 iterations. On the other hand, if the cumulative $\Delta\Phi_{max}$ decreases by the same critical value, the damping factor will be decreased by 0.1. In addition, the damping factor is also restricted to be within a minimum and a maximum value. This method of changing the damping factor during iterations appears to work well in the transonic nonuniform flow.

In direct optimization, the starting damping factor usually should be less because the initial Φ values are from the converged solution of a previous analysis run. Typically, a value equal to half of that used in the initial analysis run would be adequate.

3.3 Over-Relaxation Factor

An over-relaxation factor is used only in the subonic region. If $\Delta\Phi_{max}$ changes sign frequently, the over-relaxation factor needs to be reduced. On the other hand, if $\Delta\Phi_{max}$ does not change sign, the factor should be increased. However, oscillatory convergence is also possible. The criteria for changing the over-relaxation factor built into the present code are that if the number of sign changes is greater than five and more than three of which are with $\Delta\Phi_{max}$ greater than twice the convergence criterion, then the factor will be decreased by 0.05. On the other hand, if the number of sign changes is less than three, it will be increased by 0.05. A maximum value of 1.7 is built into the program, and a minimum value is to be input.

3.4 Convergence Criterion

In the nonuniform flow, the equation has been shown to be nondimensionalized with respect to the stagnation speed of sound. Therefore, the convergence criterion should be more stringent for the nonuniform flow. However, if a too stringent convergence criterion is used in the coarse grids, divergence may occur when the grids are halved. Therefore, a relaxed convergence criterion is usually needed for coarse and medium grids.

On the other hand, at the beginning of iterations for each grid system, Φ values are usually far from being correct. It tends to work better if the convergence criterion is relaxed initially until the convergence reaches a certain stage (called an acceptable region in the code). Then the criterion is tightened until the convergence reaches the next stage (called a stable region in the code). After the stable region has been reached, inverse design, viscous interaction, update of rotation function and airfoil shape in the inverse design can be started.

In direct optimization, the original convergence criterion is multiplied by 2.5 to reduce the computing time. The final convergence is achieved by a separate run in the analysis mode using the converged Φ values in the last run.

All of the aforementioned ideas have been built into the code.

3.5 Under-Relaxation Factor for Airfoil Shape in Inverse Design

Subroutine SHAPE is used to update the airfoil shape in the inverse design. Relaxation solution may diverge if the shape is changed too much during the first few updates. An under-relaxation factor can take care of divergence. A maximum value of 1.0 and a minimum value of 0.4 are built into the code. If the shape change increases by more than 1.0×10^{-4}, the relaxation factor is decreased by 0.05. On the other hand, if the shape change decreases by more than 1.0×10^{-4}, the factor is increased by 0.05.

3.6 Under-Relaxation Factor for Boundary Layer Displacement Thickness

This factor was found to be important to the final convergence. This factor should be small, such as 0.20, to avoid oscillation in the modified airfoil shape and thus the values of Φ.

In direct optimization, this factor is set to one half of its input value.

4. NUMERICAL RESULTS AND DISCUSSIONS

4.1 Program Validation

A Joukowsky airfoil in incompressible uniform flow was used for comparison with the exact solution, Carlson's code (Ref. 42), and Chow's results (Ref. 19). Note that Carlson's code is based on disturbance velocity potential. The resulting pressure distribution is plotted in Figure 4. The present theory agrees well with Carlson's formulation with a slight discrepancy near the leading and trailing edges. The difference in the present results from those in Reference 19 may be caused by compressibility effect and different numerical techniques. The calculated lift coefficients at $\alpha = 0$ are compared in the following table.

Method	Exact	Present	Carlson	Chow, et al.
$(c_\ell)_{\alpha=0}$	0.6943	0.7117	0.7147	0.7233

It can be seen that the present result is consistent with others.

For a nonuniform flow case, the pressure distribution is compared in Figure 5. The present results show more negative C_p nearly everywhere than those of Reference 19, again perhaps because of compressibility effect. The corresponding predicted lift coefficients based on maximum free-stream dynamic pressure are as follows:

Method	Present	Chow, et al.
$(c_\ell)_{\alpha=0}$	0.6547	0.6188

4.2 A Parametric Study in Transonic Nonuniform Flow

The following results are based on the velocity profile measured at Lewis Research Center and the location of the airfoil relative to the propfan slipstream center taken to be that of a test configuration used at Langley Research Center as shown in Figure 6. If the airfoil is decomposed into a thickness part and a camber part, the thickness of a NASA supercritical airfoil can be varied to see its influence on the airfoil characteristics. This study is needed in choosing proper pressure distributions for airfoil design. Since results are more realistic to include boundary layer in the computation, both cases are run and compared. Cases with boundary layer interaction will be called the interaction cases, and those without are called inviscid cases here.

In Figures 7(a)-(d), the effect of thickness variation within ±25 percent for both inviscid and viscous cases are plotted. The angle of attack is zero. It is seen that the lift coefficients increase almost linearly with decreasing thickness. The drag coefficients increase with increasing thickness, and the pitching moment coefficients become more negative with increasing thickness. The lift-to-drag ratios increase with decrease in thickness. Inviscid results indicate higher lift-drag ratios, much higher lift coefficients and higher drag coefficients. It also means more negative pitching moment coefficients. These characteristics can be understood better by plotting the corresponding pressure distributions in Figures 8(a)-(d). From

Figures 8(a) and 8(b), it is seen that as the thickness is decreased, the shock strength is reduced and the loading tends to shift forward to make C_m more positive [Figure 7(c)]. The inviscid calculation shows higher and sharper trailing-edge pressure peaks and hence higher shock strength [Figures 8(c) and 8(d)].

The effect of camber is plotted in Figures 9(a)-(d). The general trend is that both lift and drag coefficients increase with increasing camber. However, there are large changes in aerodynamic characteristics for camber changes of 10 to 15%. In an inviscid flow, a large change occurs when the camber is decreased. On the other hand, in the viscous flow increasing camber tends to cause the sharp change. Examination of pressure distribution [Figures 10(a)-(d)] reveals that these abrupt changes are caused by shifting of shock positions and strengths.

The airfoil location relative to the slipstream is an important issue in propulsion integration. Since the swirl effect has been found to be important in three-dimensional experiments, it is of interest to examine this effect in the present two-dimensional flow. Note that the swirl effect is accounted for by an incremental angle of attack inside the slipstream. The locations of airfoil in the slipstream to be examined are illustrated in Figure 11. The results are presented in Figures 12(a)-(d). It is seen that the swirl effect is minor in two-dimensional cases. In Reference 9, the swirl velocity was shown to be converted into side velocity as the wing is approached. The nacelle used in the experiment also induced side velocity and thus the three-dimensional boundary layer effect. Since the side velocity does not exist in a two-dimensional model, the airfoil will not experience the resulting three-dimensional boundary layer effect. It follows that the swirl effect is decreased.

When the airfoil is above the slipstream center, both lift and drag decrease; but the drag decreases faster. Thus the lift-drag ratio increases greatly. Pitching moment coefficients become more positive. The pressure distribution of some selected vertical locations is plotted in Figures 13(a) and (b). It is seen that the pressure distribution is closer to that in a uniform flow when the airfoil moves away from the slipstream center in the lower half plane. From Figure 13(a), it is seen that as y/R becomes more negative, the shock strength on the upper surface tends to be decreased. On the other hand, if y/R becomes more positive, not only does the upper-surface shock remain strong, but also a lower-surface shock tends to be generated. This is expected because the velocity on the airfoil lower surface will be increased by the slipstream.

4.3 Inverse Design

The inverse design process can be described as follows:

(1) Specify a pressure distribution based on the backward finite difference (to be called the "backward" pressure) and an initial airfoil shape. Note that the design

process in the Carlson's code is formulated in terms of the "backward" pressure.

(2) The final "backward" pressure and the pressure based on the central difference (to be called the "central" pressure) are obtained together with a shape which includes a boundary layer. This shape will be called the initial design shape (i.e. outer shape) here. The aerodynamic characteristics based on this outer shape are designated as "design" in figures 14-16.

(3) The design shape is obtained by subtracting a boundary layer from the initial design shape.

(4) Input the design shape in the interaction analysis mode to obtain a more reliable boundary layer, and hence the pressure distribution. The design shape plus this boundary layer forms the "modified" shape. Its corresponding "central" pressure distribution will be called the "viscous" pressure. The aerodynamic characteristics based on interaction analysis are designated as "analysis" in Figure 15.

Different pressure distributions for inverse design are plotted in Figure 14. For an ideal situation, the specified pressure should be identical to the "backward" pressure. In this inverse design this is not satisfied near the trailing edge due to the large pressure gradient caused by the shock. There is some discrepancy near the nose. Usually, the "central" pressure distributions are close to the "backward" pressure values for smooth pressure distributions. The difference between "central" pressure and "viscous" pressure results from the different boundary layers. The resulting design shown in Figures 15 and 16 indicates that a 7.5 percent decrease in maximum thickness results in a 16.5 percent increase in lift-drag ratio. However, the trailing-edge thickness is considered too thick to be desirable. However, it is very difficult to specify a better pressure distribution to realize a better performance, and at the same time control the trailing-edge thickness. Therefore, an approach based on direct optimization will be employed in the following.

4.4 Direct Optimization

Direct optimization is achieved by integrating the analysis code with an optimizer. The problem formulation was described in Section 2.5. Although it takes many iterations to obtain a converged solution, it does not need an experienced person to do the job.

For the flow condition shown in Figure 6, a NASA supercritical airfoil is used as an input shape. Seven Fourier coefficients for both upper and lower surfaces are chosen (see Equation 39). That is, there are 14 design variables. The front 5% of the nose region is kept unchanged in the optimization. The results show that a 4 percent decrease in thickness results in a gain of 22 percent in lift-drag ratio (Figure 17). This should be compared with a direct thickness reduction from which the same gain in L/D can be achieved only by a reduction of thickness of about 17.5% [Figure 7(d)]. The improvement appears to lie in a small thickness increase in the nose region to accelerate the flow and a flatter mid upper surface to reduce the shock strength. On the lower surface, two weak supersonic regions appear.

Based on extensive numerical experience in designing an airfoil in transonic nonuniform flow, the method of direct optimization is found to be much esier to use and has a better chance to design a good airfoil in comparison with the inverse method. However, it has the disadvantage of requiring long computer CPU time. On the other hand, the CPU time to determine an airfoil shape in the inverse method is relatively small. The main disadvantage in the inverse method lies in the difficulty of specifying a good pressure distribution for low drag at a given lift coefficient and at the same time controlling the thickness of the trailing edge.

5. CONCLUSIONS

A nonuniform transonic airfoil code capable of performing analysis, inverse design and direct optimization was developed. Problems involving numerical stability, convergence, divergence and solution oscillations were discussed. Application of the code to an airfoil immersed in a transonic propfan slipstream indicated that decrease in thickness would increase the lift and lift-drag ratio and make the pitching moment more negative. Increase in camber, however, tended to decrease the lift-drag ratio in a nonlinear manner. The nonlinearity arose from the rapid shift in shock locations when camber was changed. Swirl effect was found to be insignificant in the present two-dimensional case. The airfoil performance tended to be better if it was located below the propfan slipstream center.

Both inverse design and direct optimization of an airfoil were conducted. It was found that the airfoil designed through the direct optimization offered a better performance resulting in a gain of 22 percent in lift-drag ratio for a reduction of 4 percent in thickness. The airfoil shape could also be better controlled than that based on the inverse design method.

6. REFERENCES

1. Rohrback, C., "A Report on the Aerodynamic Design and Windtunnel Test of a Propfan Model." AIAA paper 76-667, July 1976.
2. Kraus, E. F., and van Abkoude, J. C., "Cost/Benefit Tradeoffs for Reducing the Energy Consumption of the Commercial Air Transportation System." Douglas Aircraft Company, NASA CR-137925, June 1976.
3. Hopkins, J. P., and Wharton, H. E., "Study of the Cost/Benefit Tradeoffs for Reducing the Energy Consumption of the Commercial Air Transportation System." Lockheed California Company, NASA CR-137927, August 1976.
4. "Energy Consumption Characteristics of Transports Using the Propfan Concept." The Boeing Commercial Airplane Company, NASA CR-137938, November 1976.
5. Dugan, J. F., Miller, B. A., Graber, E. J., and Sagerser, D. A., "The NASA High-Speed Turboprop Program." SAE paper 801120.
6. Welge, H. R., and Crowder, J. P., "Simulated Propeller Slipstream Effects on a Supercritical Wing." NASA CR-152138, June 1978.
7. Bencze, D. P., Smith, R. C., Welge, H. R., and Crowder, J. P., "Propeller Slipstream Wing Interaction at Mach 0.8." SAE paper 780997.

8. Boctor, M. L., Clay, C. W., and Watson, C. F., "An Analysis of Propfan/Airframe Aerodynamic Integration." NASA CR-152186, October 1978.

9. Welge, H. R., "Propfan Integration at Cruise Speeds." AGARD CP-301, paper 33, May 1981.

10. Welge, H. R., Neuhart, D. H., and Dahlin, J. A., "Analysis of Mach 0.8 Turboprop Slipstream Wing/Nacelle Interaction." NASA CR-166214, Douglas Aircraft Company, Long Beach, California, August 1981.

11. Smith, R. C.; and Levin, A. D.: "Propfan Installation Aerodynamics of a Supercritical Swept Wing Transport Configuration." AIAA/SAE/ASME 17th Joint Propulsion Conference, July 27-29, 1981, Colorado Springs, Colorado, AIAA paper 81-1563.

12. Levin, A. D.; and Smith, R. C.: "Propfan Propulsion Integration Test Techniques." AIAA paper 82-0577, 1982.

13. Samant, S. S.; Hultman, D.; Lines, T. R.; Yu, N. J., and Rubbert, P. E.: "Propfan Nacelle Installations at Transonic Speeds." NASA CR-166376, October 1982.

14. Levin, A. D., and Smith, R. C., "Installed Nacelle Drag-Improvement Tests of a M = 0.8 Turboprop Transport Configuration." NASA TM-84302, January 1983.

15. Bartlett, G. R., "An Experimental Investigation of Propfan Installations on an Unswept Supercritical Wing." M.S. Thesis, George Washington University, August 1983.

16. Koning, C., "Influence of the Propeller on Other Parts of the Airplane." Aerodynamic Theory, Vol. IV, Springer-Verlag, Berlin, 1935.

17. Ferrari, C., "Propeller and Wing Interaction at Subsonic Speeds," in Aerodynamic Components of Aircraft at High Speed. Edited by A. F. Donovan and H. R. Lawrence, Sec. C, Princeton University Press, Princeton, New Jersey, 1957, Chapter 3.

18. Rethorst, S., "Aerodynamics of Nonuniform Flow as Related to an Airfoil Extending Through a Circular Jet." Journal of the Aeronautical Science, January 1958, pp. 11-28.

19. Chow, F., Krause, E., Liu, C. H., and Mao, J., "Numerical Investigations of an Airfoil in a Nonuniform Stream." Journal of Aircraft, Vol. 7, No. 6, November-December 1970, pp. 531-537.

20. Jameson, A., "Analysis of Wing Slipstream Flow Interaction." NASA CR-1632, August 1970.

21. Ting, L., Liu, C. H., and Kleinstein, G., "Interference of Wing and Multipropeller." AIAA Journal, Vol. 10, No. 7, July 1972, pp. 906-914.

22. Shollenberger, C. A., "Three-Dimensional Wing/Jet Interaction Analysis Including Jet Distortion Influences." Journal of Aircraft, Vol. 12, No. 9, September 1975, pp. 706-713.

23. Lan, C. E., "Wing-Slipstream Interaction with Mach Number Nonuniformity." Journal of Aircraft, Vol. 12, No. 10, October 1975, pp. 759-760.

24. Lan, C. E., "A Quasi-Vortex-Lattice Method in Thin Wing Theory." Journal of Aircraft, Vol. 11, No. 9, September 1974, pp. 518-527.

25. Chin, W. C., "Thin Airfoil Theory for Planar Inviscid Shear Flow." Journal of Applied Mechanics, ASME, Vol. 51, March 1984, pp. 19-26.

26. Rizk, M. H., "Propeller Slipstream/Wing Interaction in the Transonic Regime." Journal of Aircraft, Vol. 18, No. 3, March 1981, pp. 184-191.

27. Samant, S. S., Yu, N. J., and Rubbert, P. E., "Transonic Flow Simulation of Propfan Configurations." AIAA paper 83-0187, January 1983.

28. Jameson, A., and Caughey, D. A., "A Finite Volume Method for Transonic Potential Flow Calculations." AIAA 3rd Computational Fluid Dynamics Conference, Albuquerque, New Mexico, June 1977.

29. Narain, J. P., "A Transonic Analysis of Propfan Slipstream Effects on a Supercritical Wing." AIAA paper 83-0186, January 1983.

30. Jameson, A., and Caughey, D. A., "Numerical Calculation of the Transonic Flow Past a Swept Wing." Courant Institute of Mathematical Sciences, New York University, COO-3077-140, June 1977. (Available as NASA CR-153297.)

31. Whitfield, D. L., and Jameson, A., "Three-Dimensional Euler Equation Simulation of Propeller-Wing Interaction in Transonic Flow." AIAA paper 83-0236, January 1983.

32. Whitfield, D. L., Swafford, T. W., and Jacocks, J. L., "Calculation of Turbulent Boundary Layers with Separated and Viscous-Inviscid Interaction." AIAA Journal, Vol. 19, No. 10, October 1980, pp. 1315-1322.

33. Brown, E. F., Brecht, T. J. F., and Walsh, K. E., "A Relaxation Solution of Transonic Nozzle Flows Including Rotational Flow Effects." Journal of Aircraft, Vol. 14, No. 10, October 1977, pp. 944-951.

34. Chaderjian, N. M., and Steger, J. L., "A Zonal Approach for the Steady Transonic Simulation of Inviscid Rotational Flow." AIAA paper 82-1927, January 1983.

35. Vanderplaats, G. N., "CONMIN-A Fortran Program for Constrained Function Optimization." NASA TM X-62282, August 1973.

36. Schouten, G., "Static Pressure in the Slipstream of a Propeller." Journal of Aircraft, Vol. 19, No. 3, March 1982, pp. 251-252.

37. Ludford, G. S. S., "The Behavior at Infinity of the Potential Function of a Two-Dimensional Subsonic Compressible Flow." Journal of Mathematical Physics, Vol. 30, October 1951, pp. 117-130.

38. Carlson, L. A., "Transonic Airfoil Flowfield Analysis Using Cartesian Coordinates." NASA CR-2577, August 1975.

39. Jameson, A., "Iterative Solution of Transonic Flow over Airfoils and Wings, Including Flows at Mach One." Communication of Pure and Applied Mathematics, Vol. 27, 1974, pp. 283-309.

40. Carlson, L. A., "Transonic Airfoil Design Using Cartesian Coordinates." NASA CR-2578, April 1976.

41. Carlson, L. A., "Transonic Airfoil Analysis and Design Using Cartesian Coordinates." Journal of Aircraft, Vol. 13, No.5, May 1976.

42. Carlson, L. A., "TRANDES: A Fortran Program for Transonic Airfoil Analysis or Design." NASA CR-2821, June 1977.

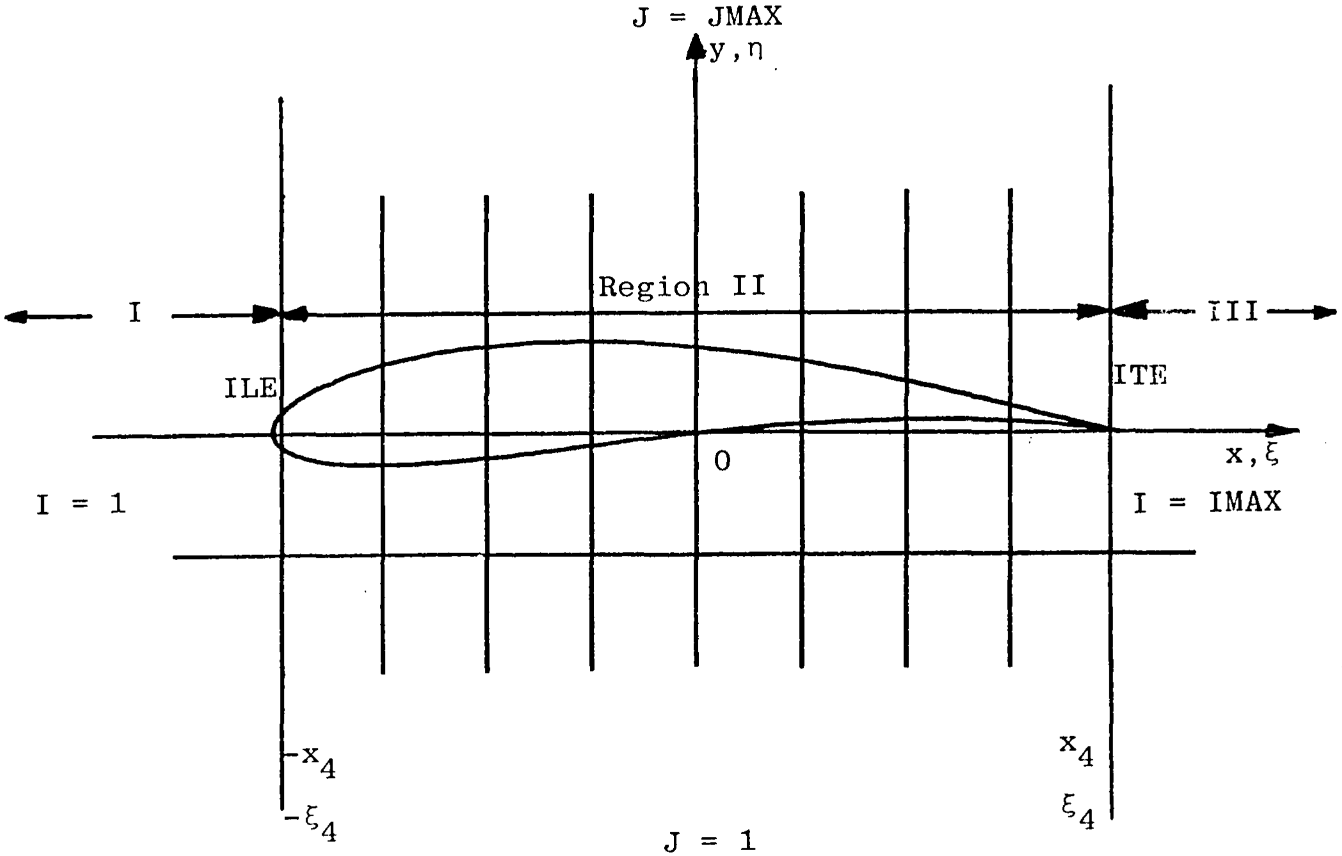

Figure 1. Flow Field Subdivision for Coordinate Stretching

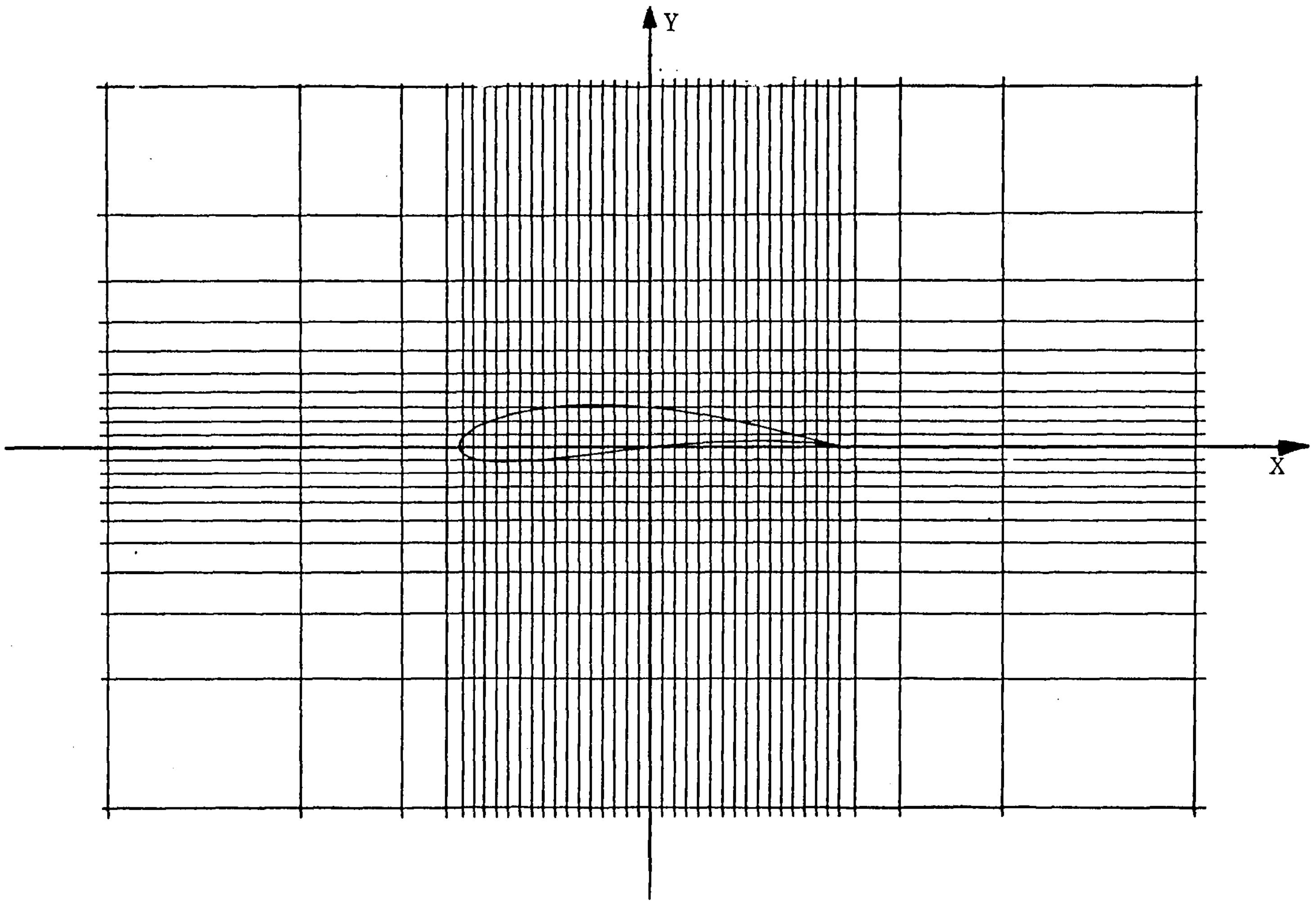

Figure 2. Typical Grid System

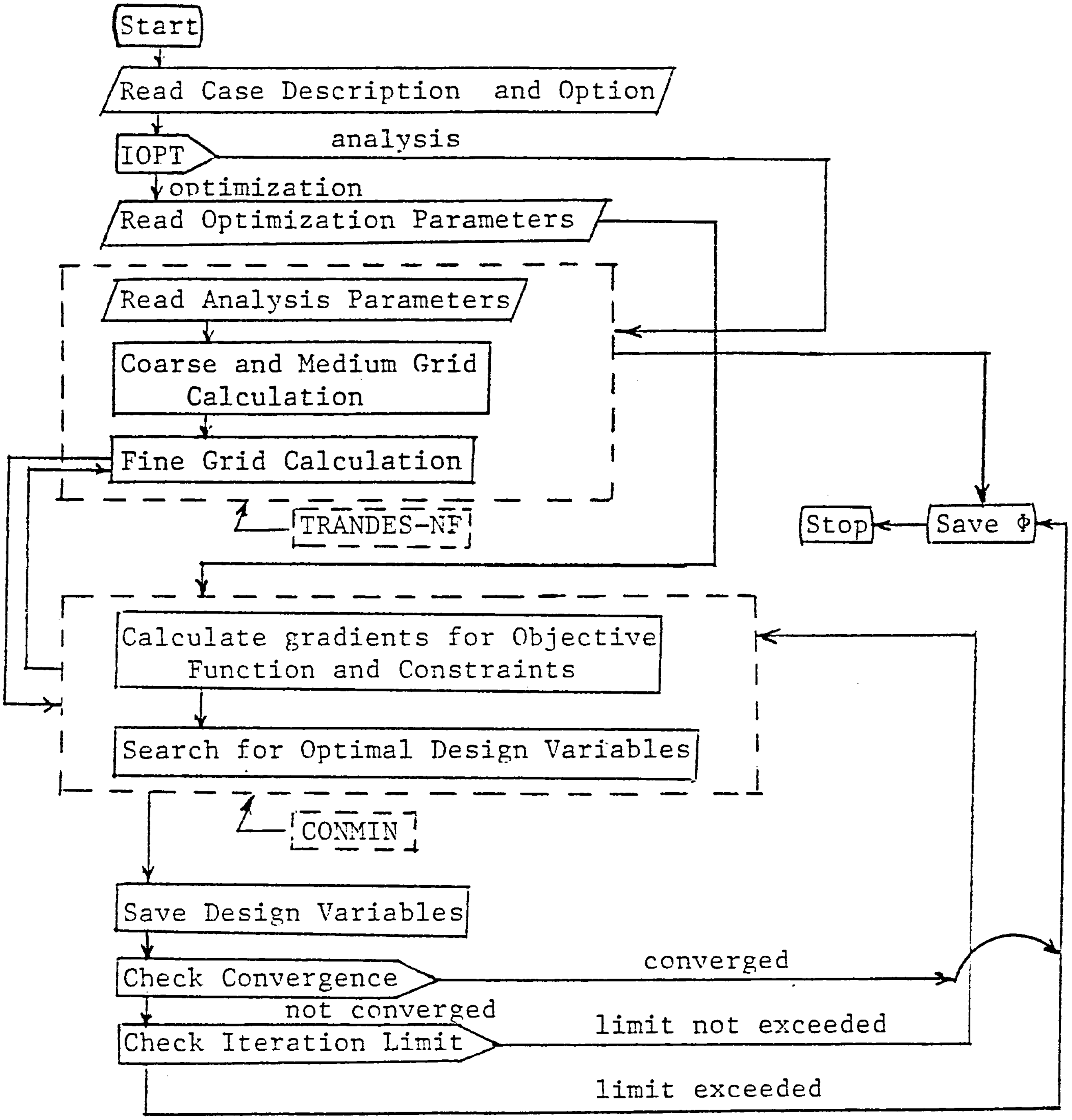

Figure 3. Flow Chart of Integrating CONMIN and TRANDESNF

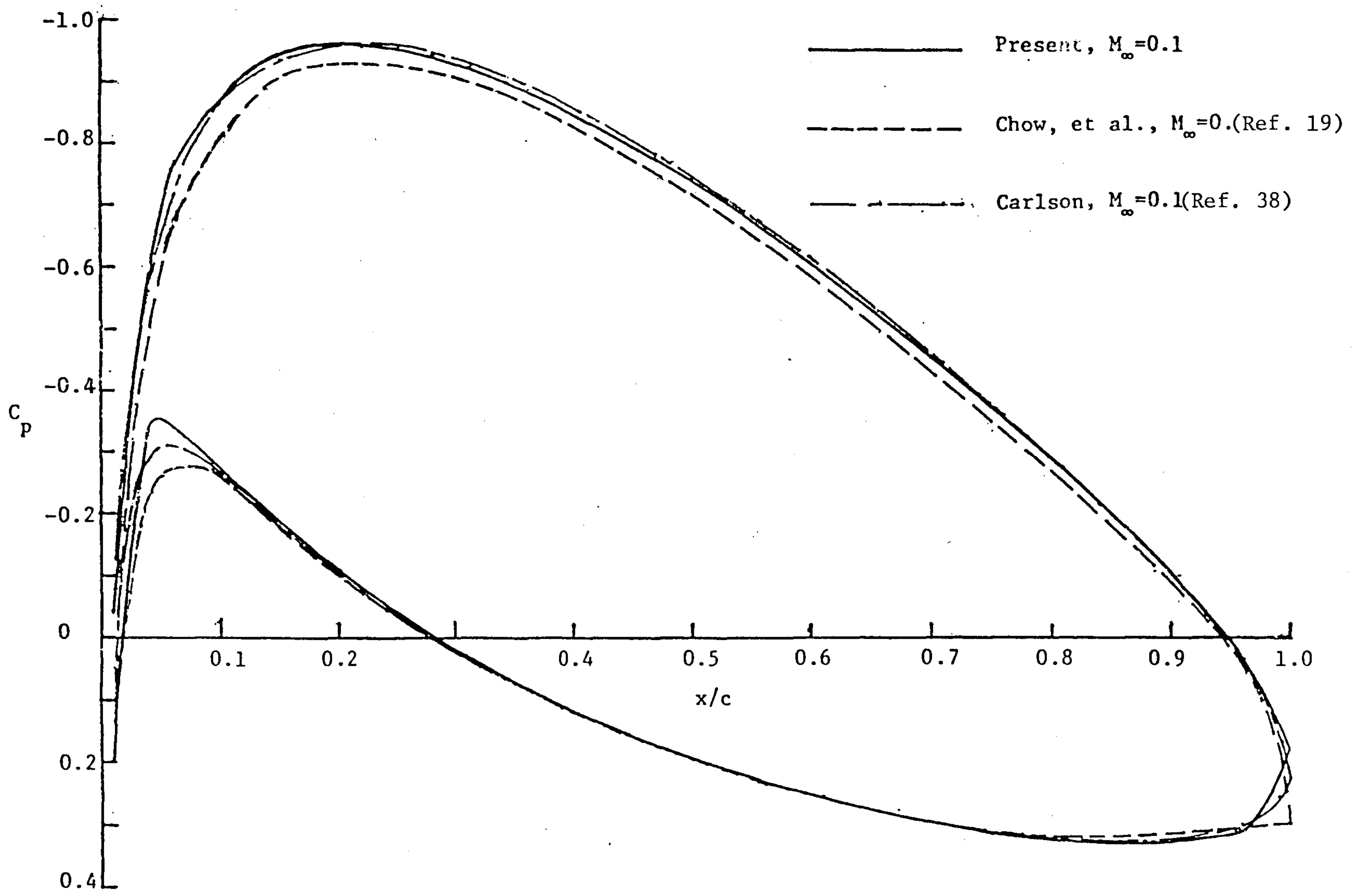

Figure 4. Pressure Distribution on a Joukowsky Airfoil in Uniform Flow at zero Angle of Attack

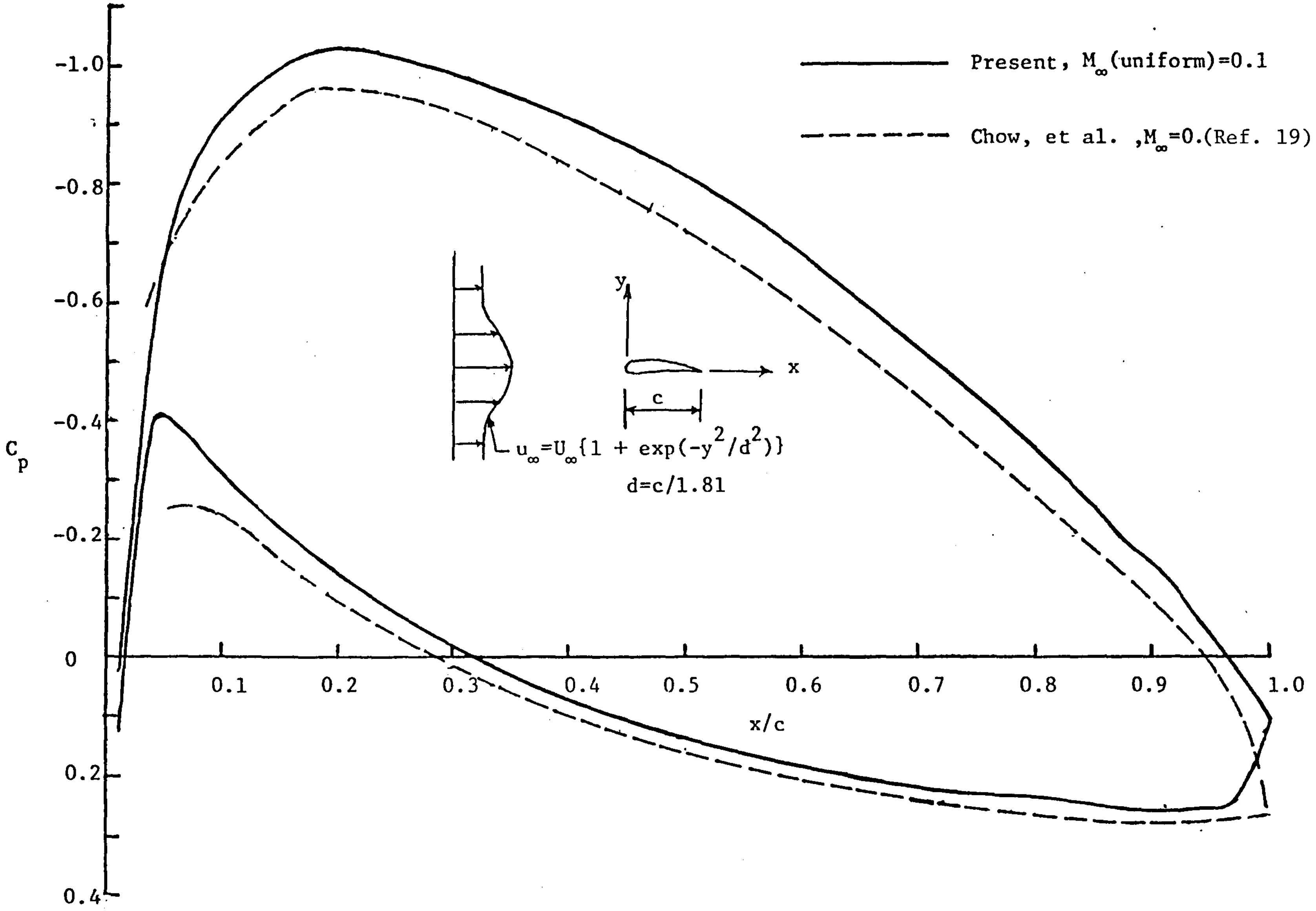

Figure 5. Pressure Distribution of a Joukowsky Airfoil in a Nonuniform Flow at Zero Angle of Attack. C_p Based on the Freestream Dynamic Pressure on the Airfoil Surface Streamline

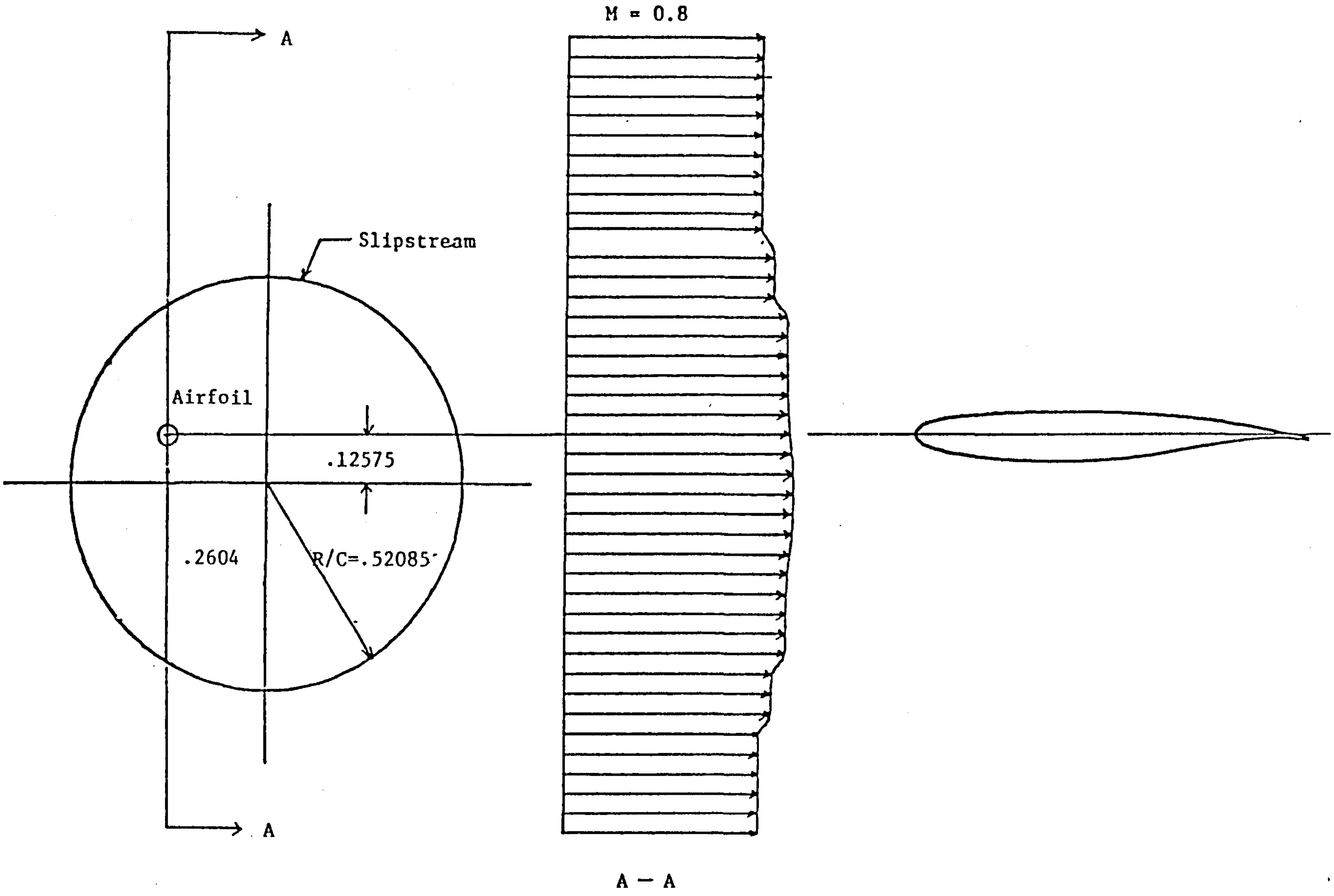

Figure 6. Mach Number Profile of a Propfan at M = 0.8 and Relative Airfoil Location

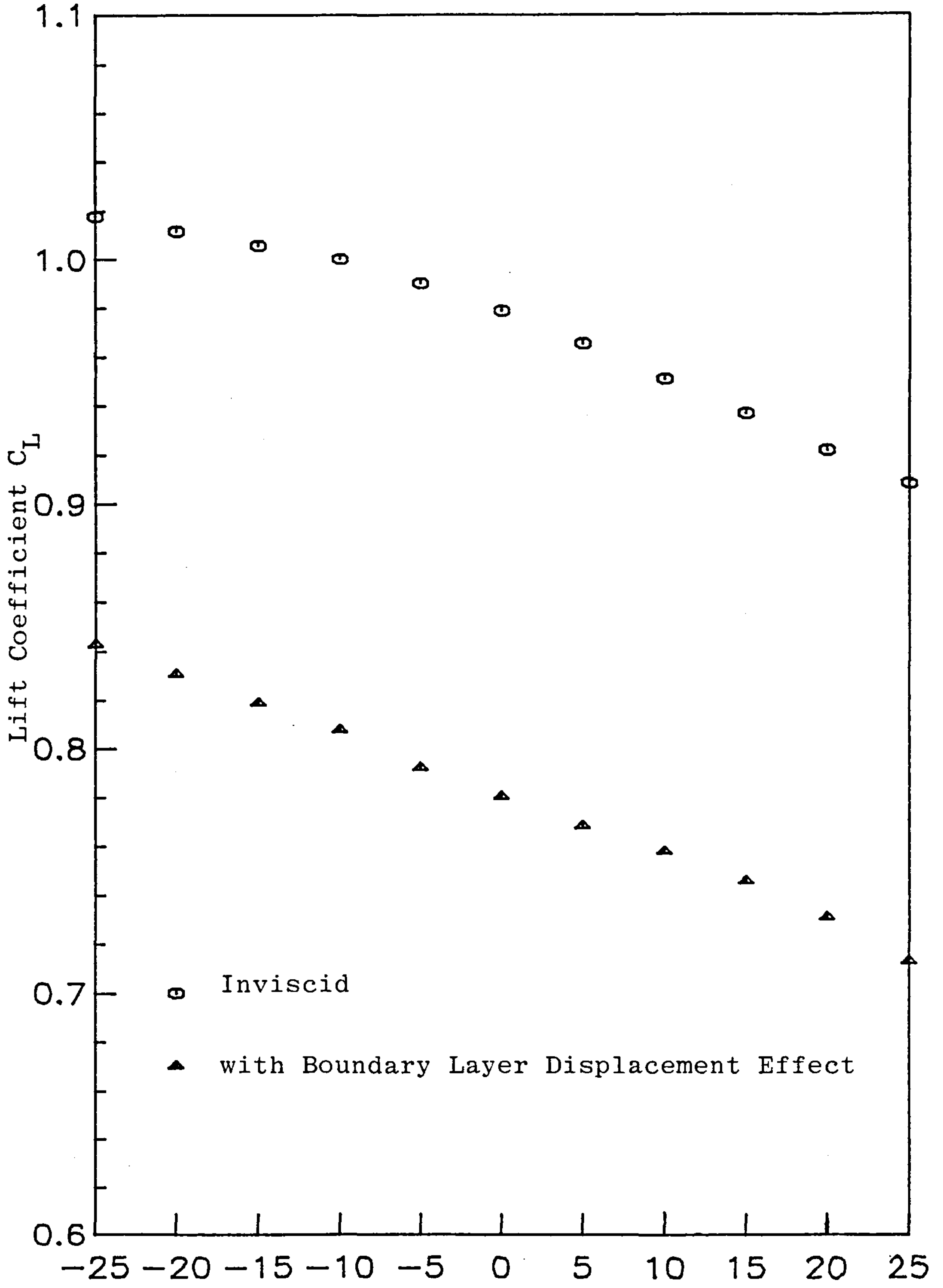

Figure 7a. Thickness Effect of a NASA Airfoil on the Lift Coefficients in a Nonuniform Flow at Zero Angle of Attack and Mach Number 0.8

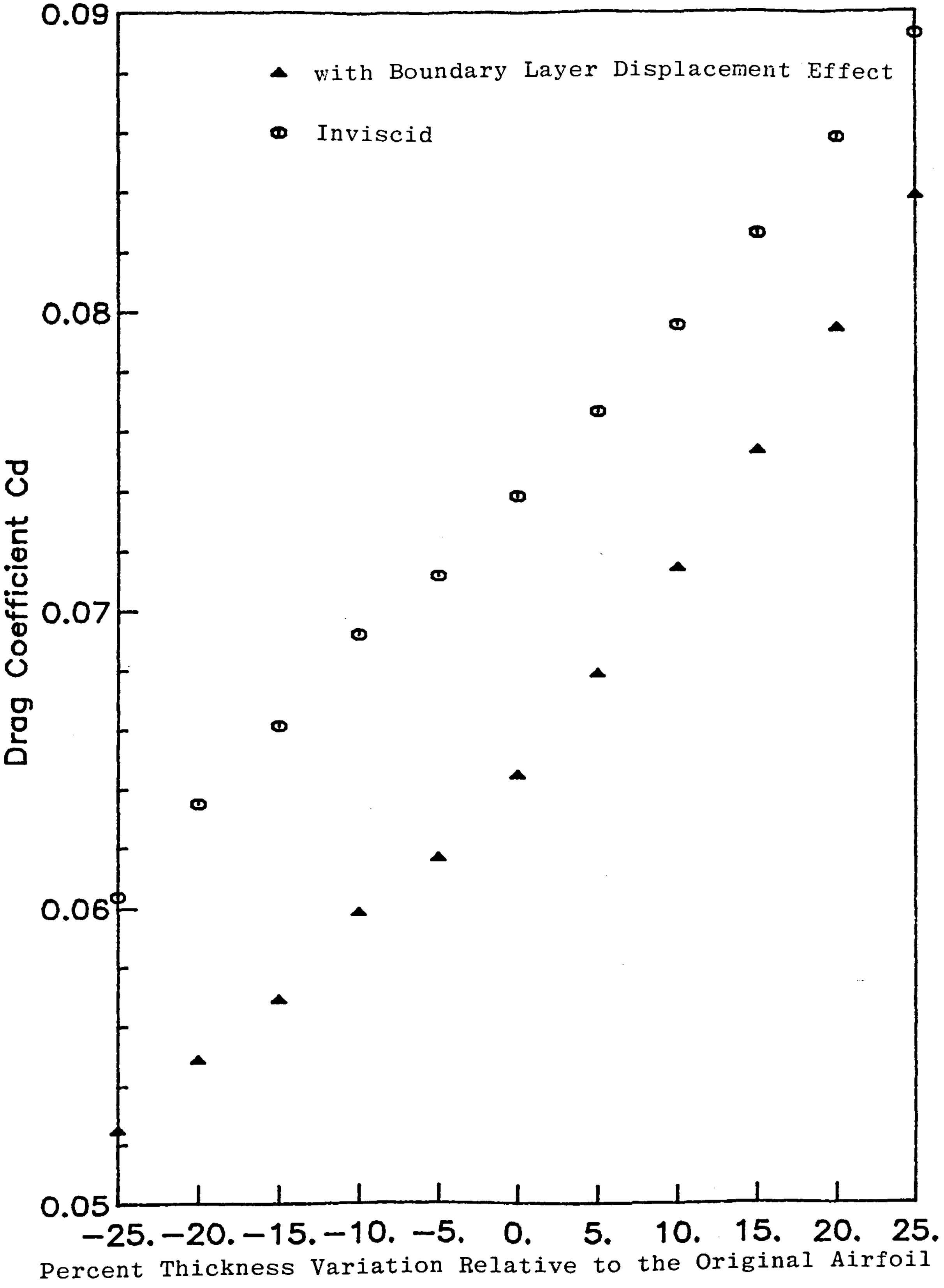

Figure 7b. Thickness Effect of a NASA Airfoil on the Drag Coefficients in a Nonuniform Flow at Zero Angle of Attack and Mach Number 0.8

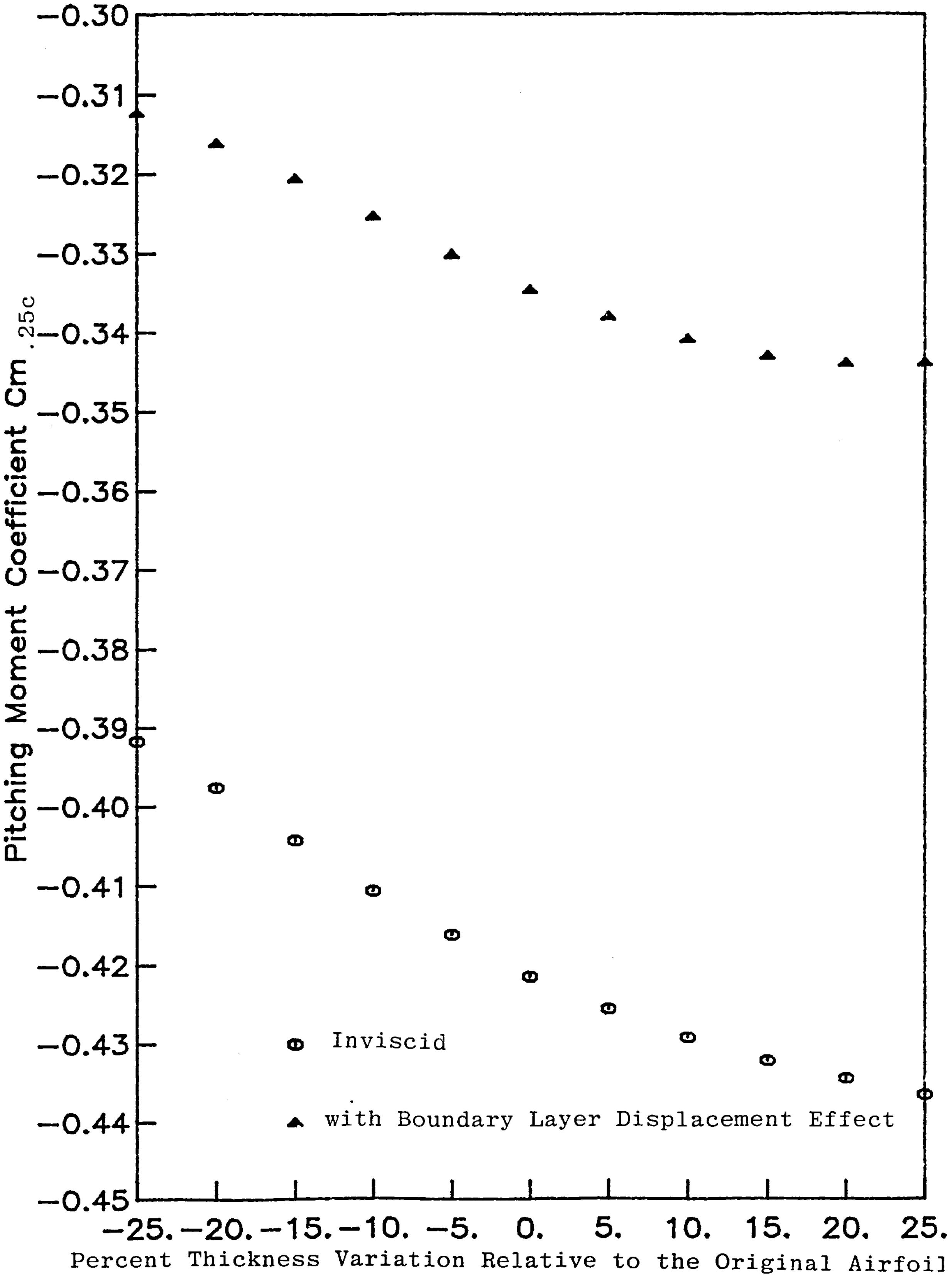

Figure 7c. Thickness Effect of a NASA Airfoil on the Pitching Moment Coefficients in a Nonuniform Flow at Zero Angle of Attack and Mach Number 0.8

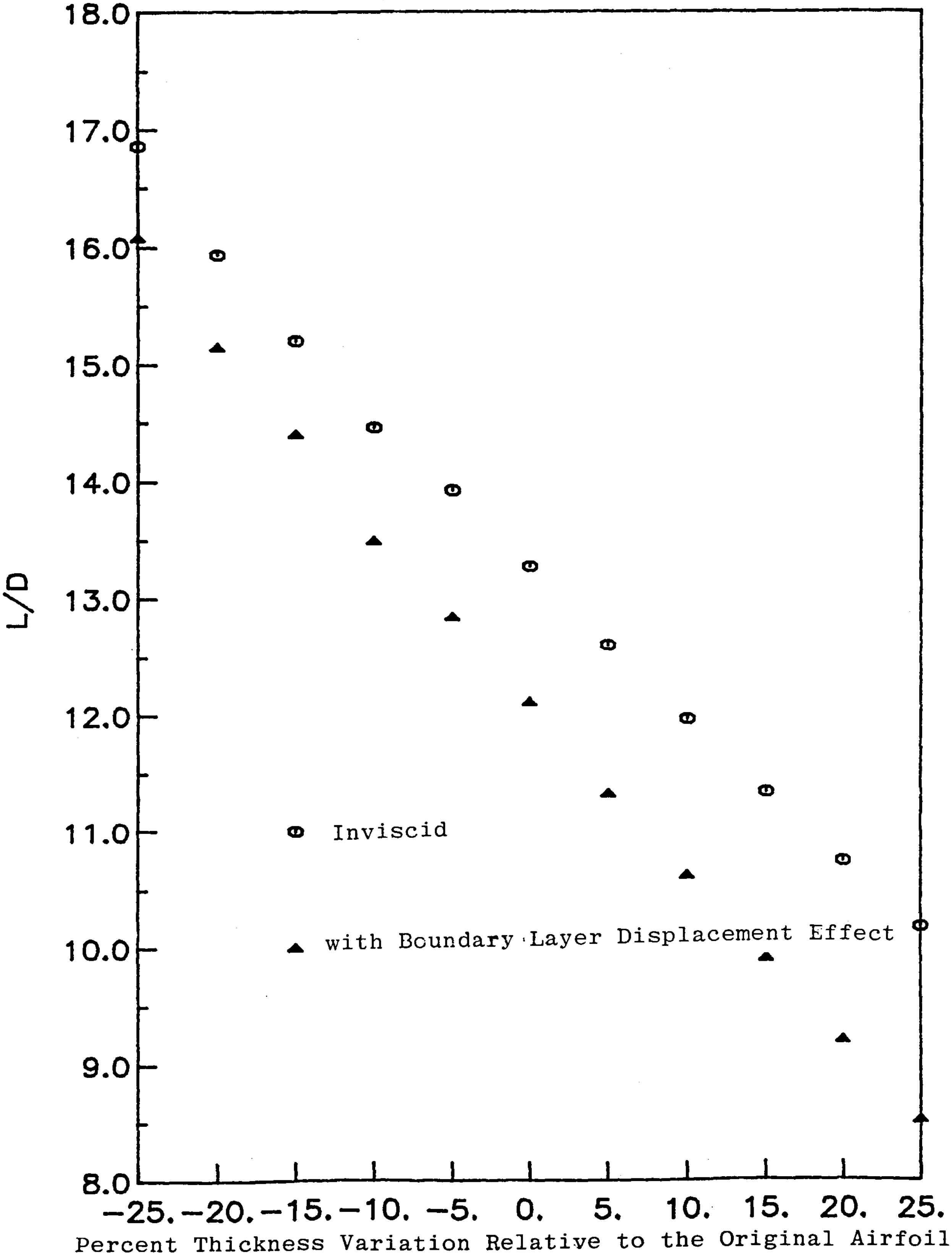

Figure 7d. Thickness Effect of a NASA Airfoil on the Lift-Drag Ratios in a Nonuniform Flow at Zero Angle of Attack and Mach Number 0.8

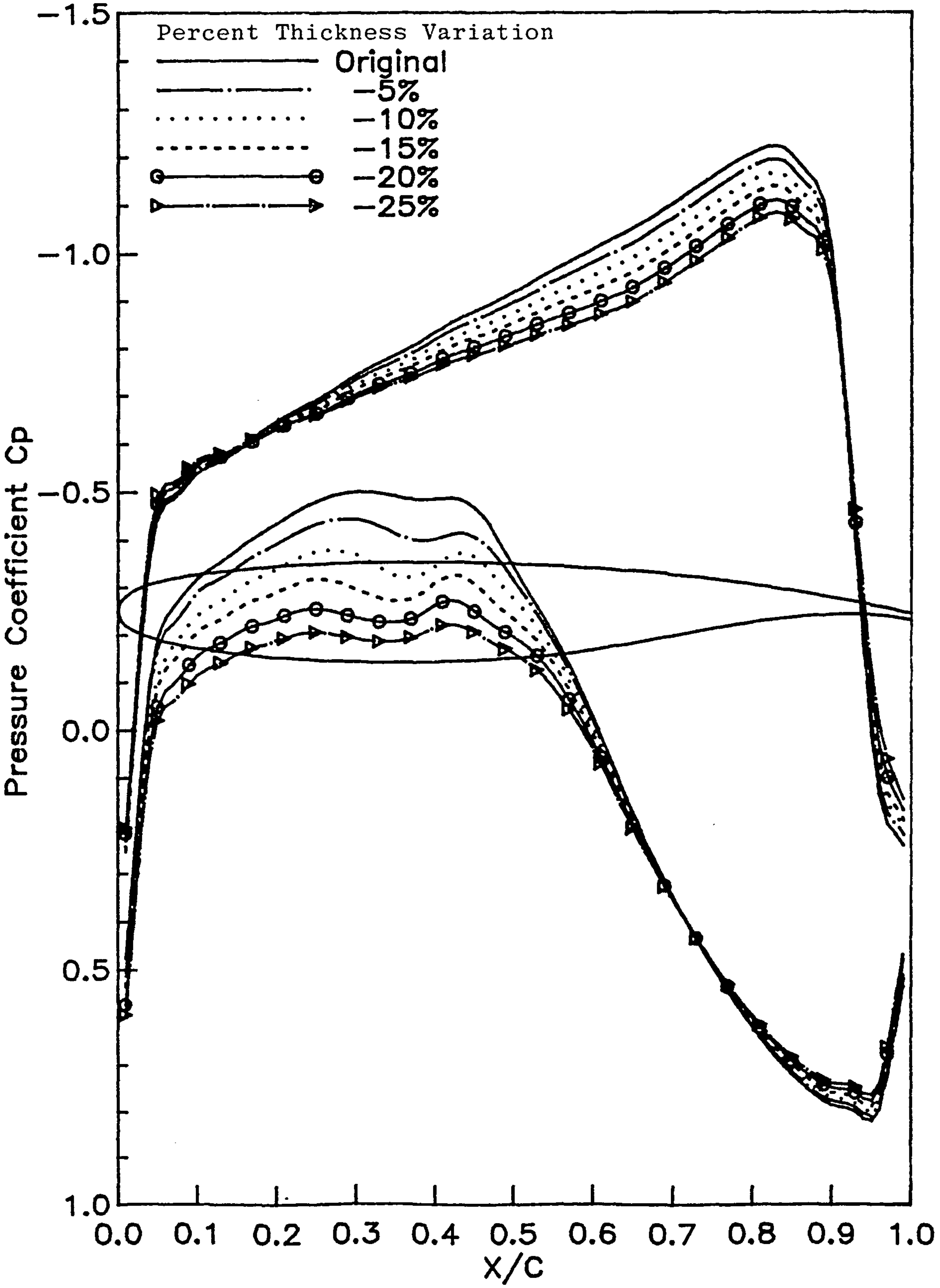

Figure 8a. Thickness Effect of a NASA Airfoil on Pressure Distributions in a Nonuniform Flow at Zero Angle of Attack and Mach Number 0.8 Including Boundary Layer Displacement Effect

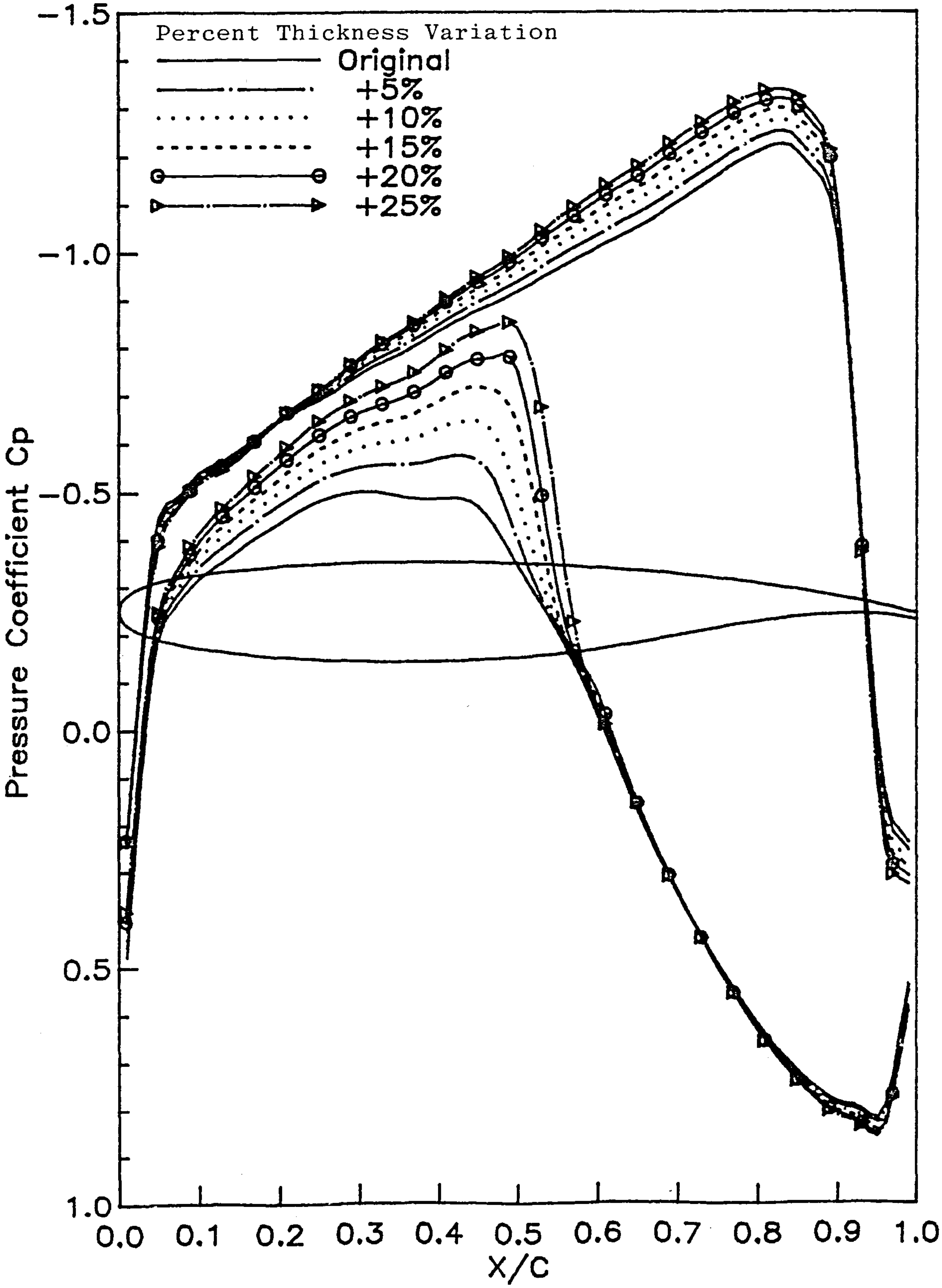

Figure 8b. Thickness Effect of a NASA Airfoil on Pressure Distributions in a Nonuniform Flow at Zero Angle of Attack and Mach Number 0.8 Including Boundary Layer Displacement Effect

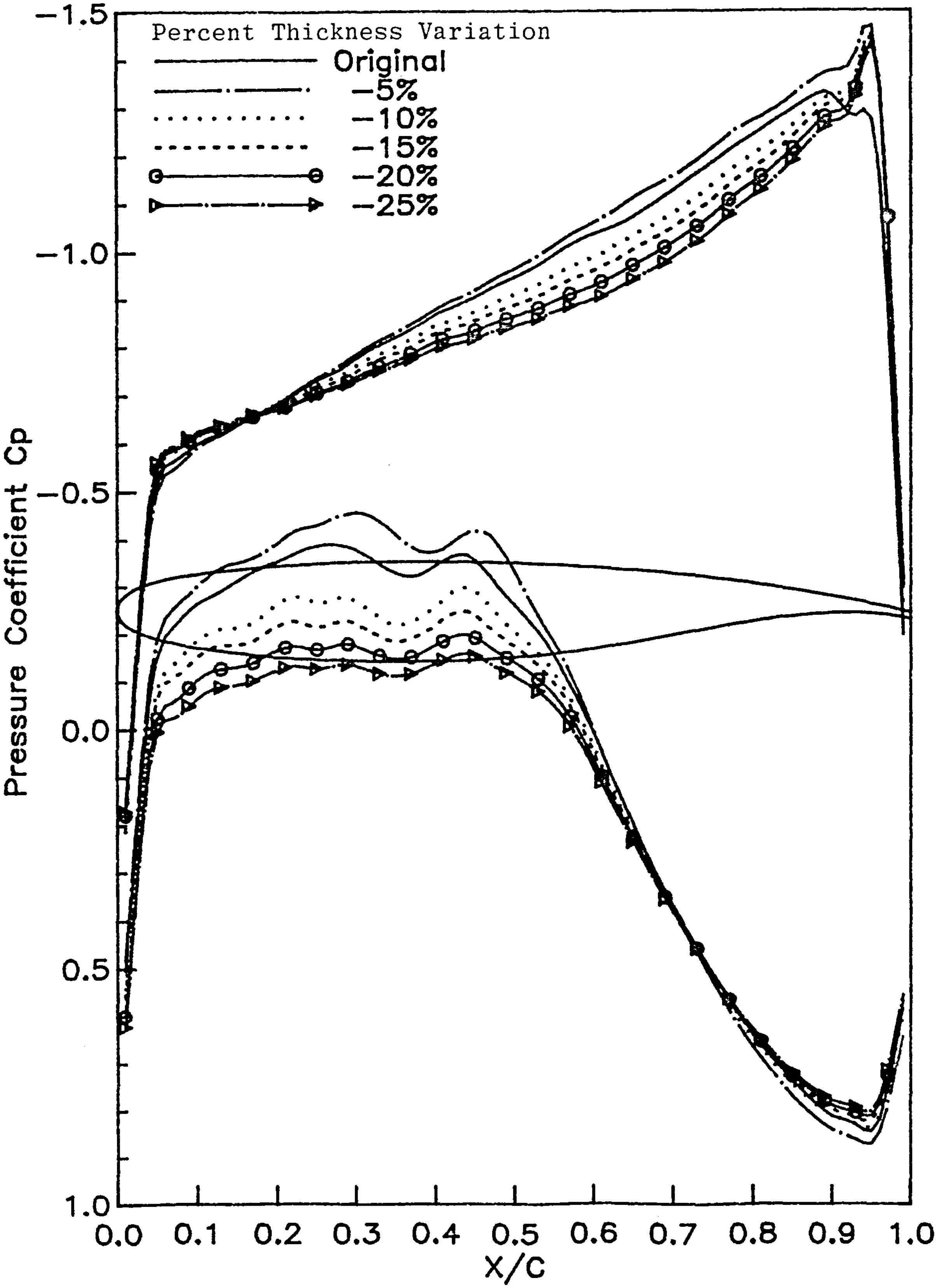

Figure 8c. Thickness Effect of a NASA Airfoil on Pressure Distributions in an Inviscid Nonuniform Flow at Zero Angle of Attack and Mach Number 0.8

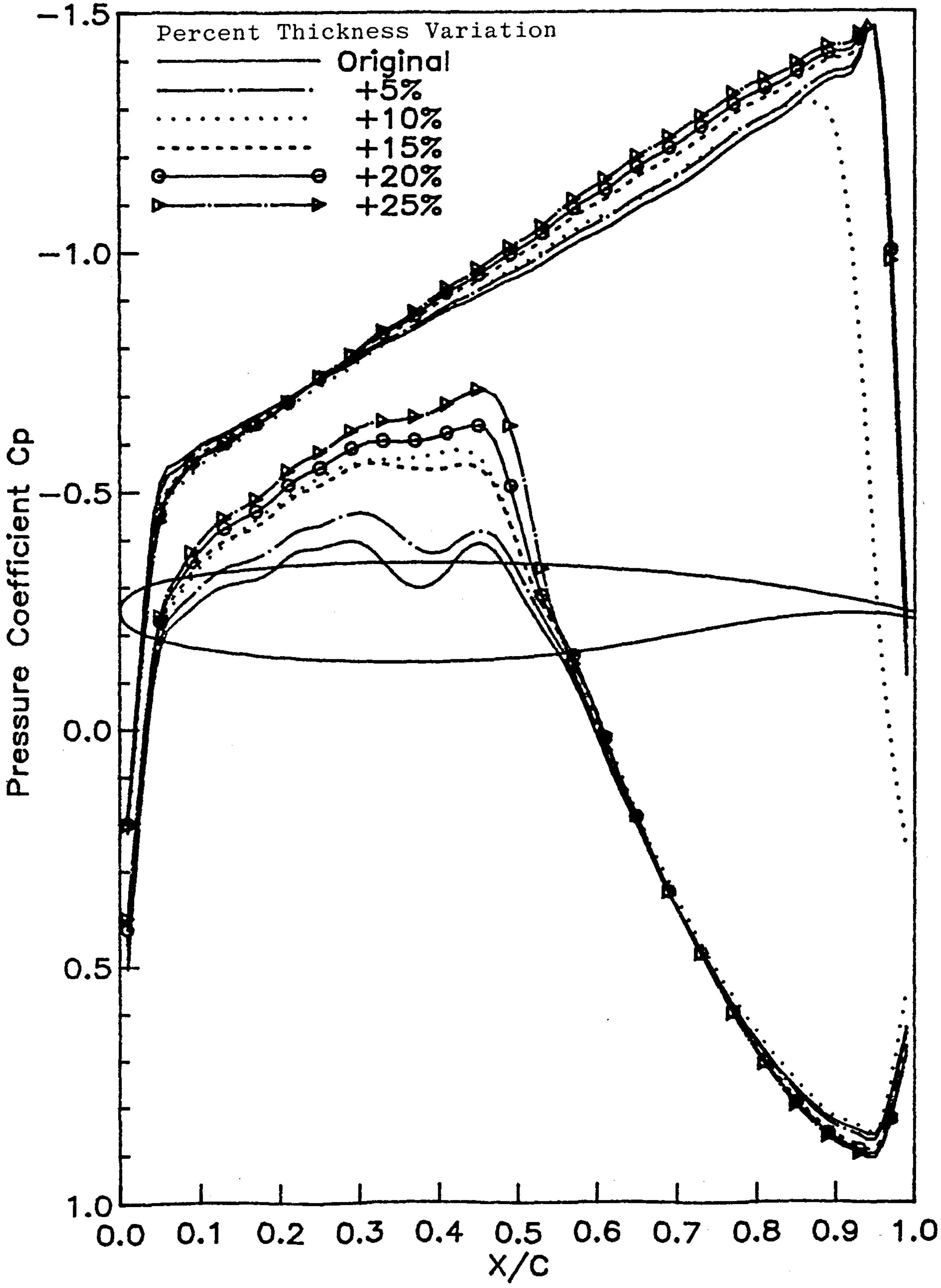

Figure 8d. Thickness Effect of a NASA Airfoil on Pressure Distributions in an Inviscid Nonuniform Flow at Zero Angle of Attack and Mach Number 0.8

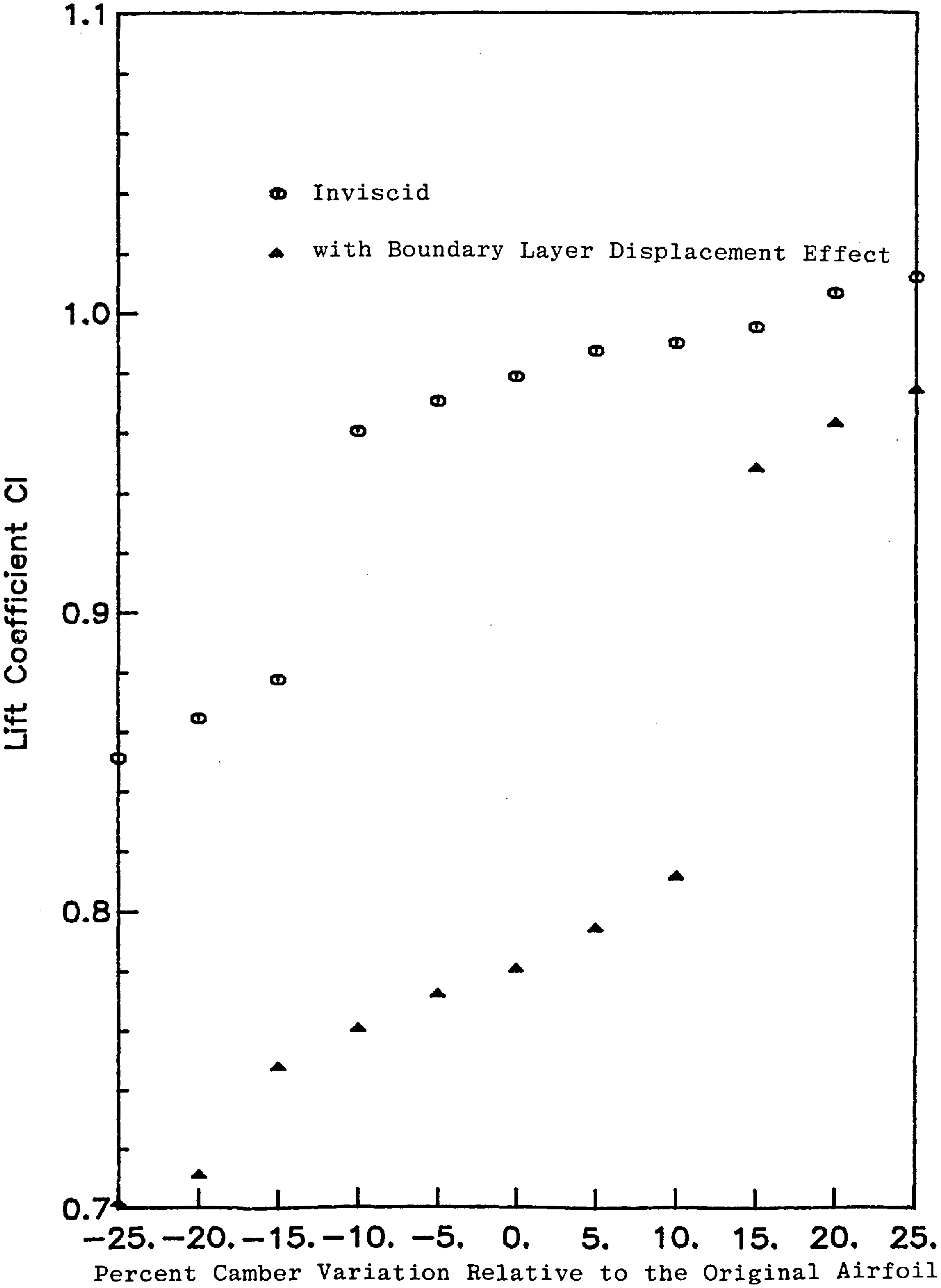

Figure 9a. Camber Effect of a NASA Airfoil on the Lift Coefficients in a Nonuniform Flow at Zero Angle of Attack and Mach Number 0.8

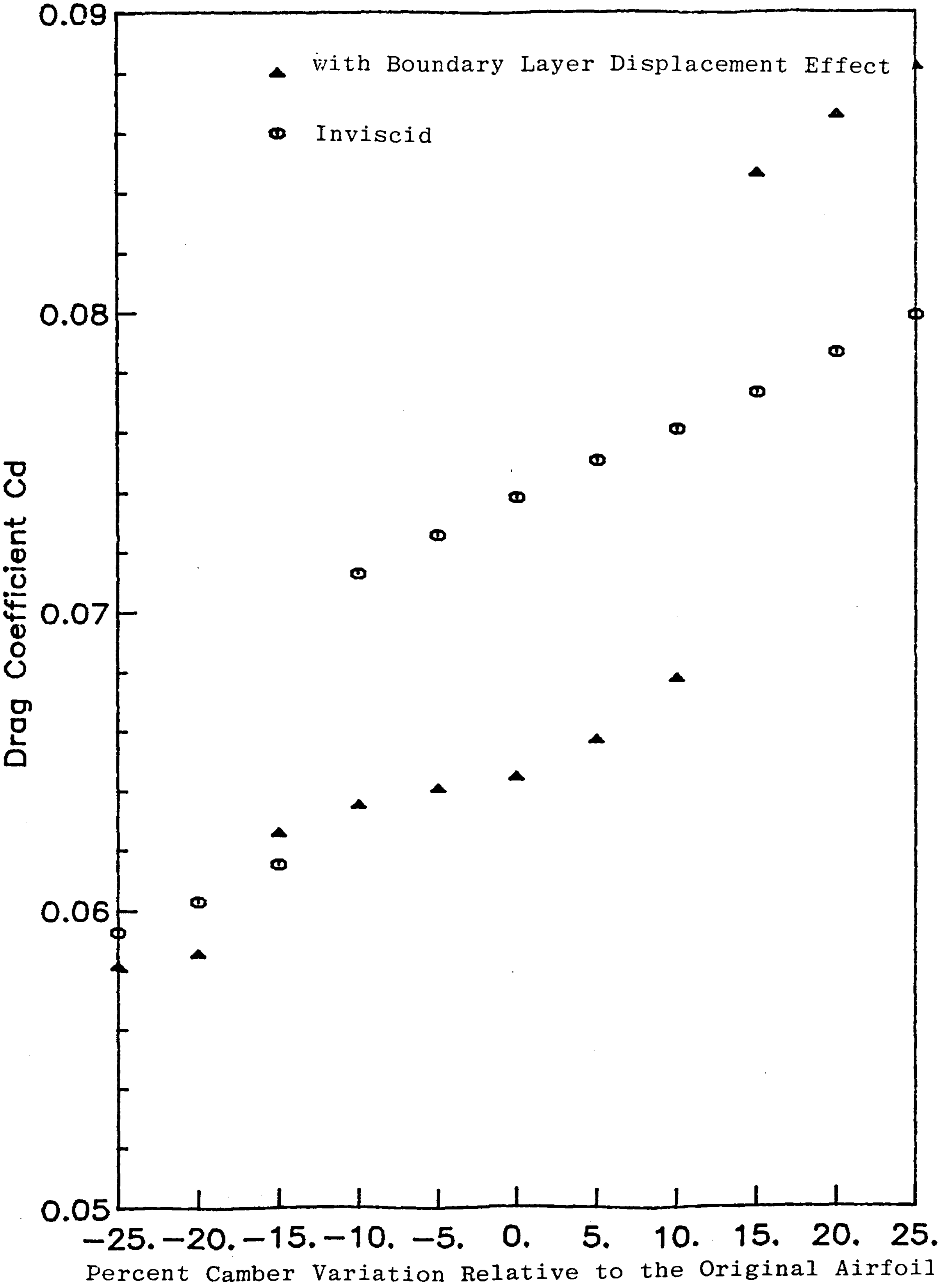

Figure 9b. Camber Effect of a NASA Airfoil on the Drag Coefficients in a Nonuniform Flow at Zero Angle of Attack and Mach Number 0.8

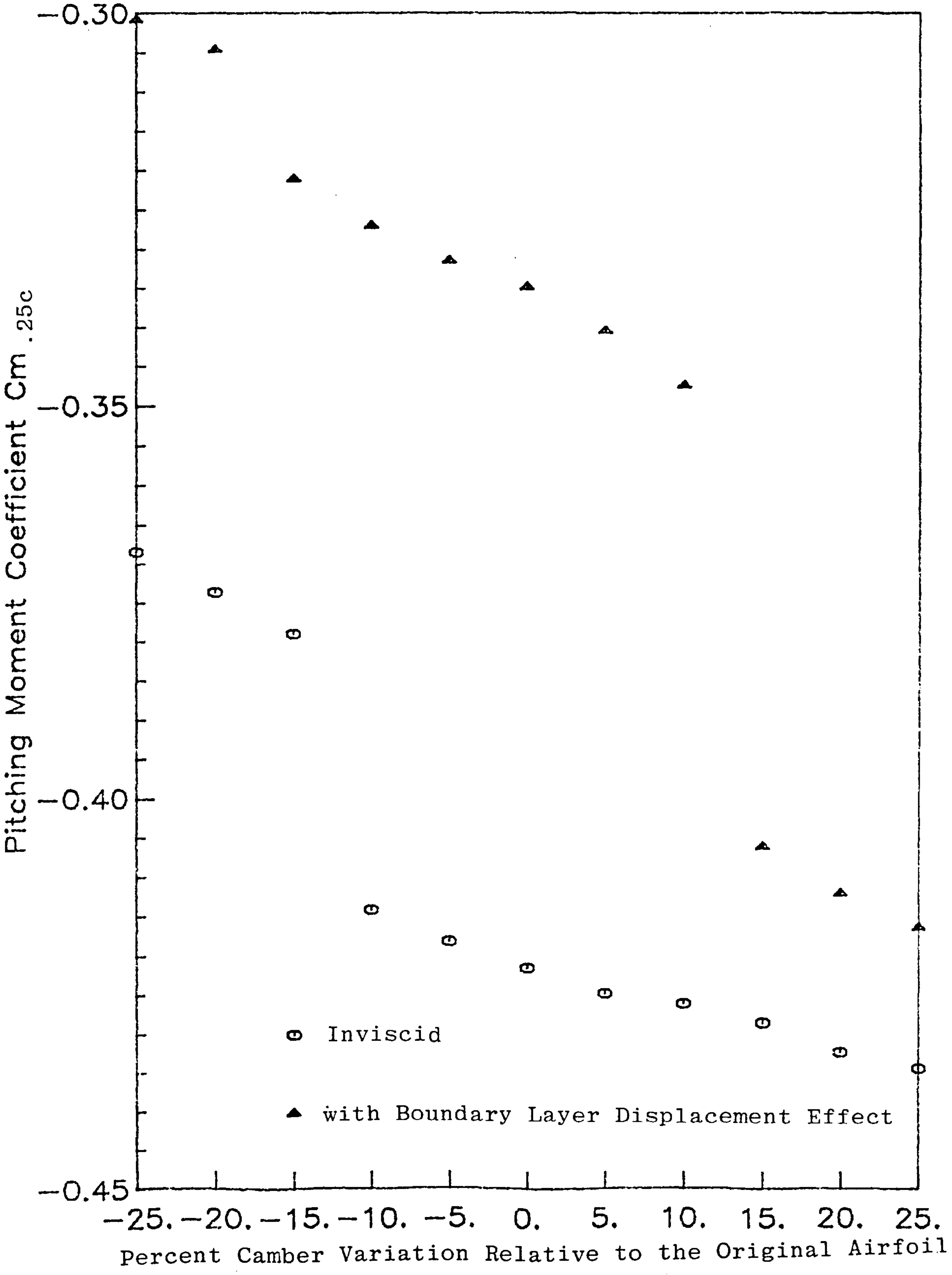

Figure 9c. Camber Effect of a NASA Airfoil on the Pitching Moment Coefficients in a Nonuniform Flow at Zero Angle of Attack and Mach Number 0.8

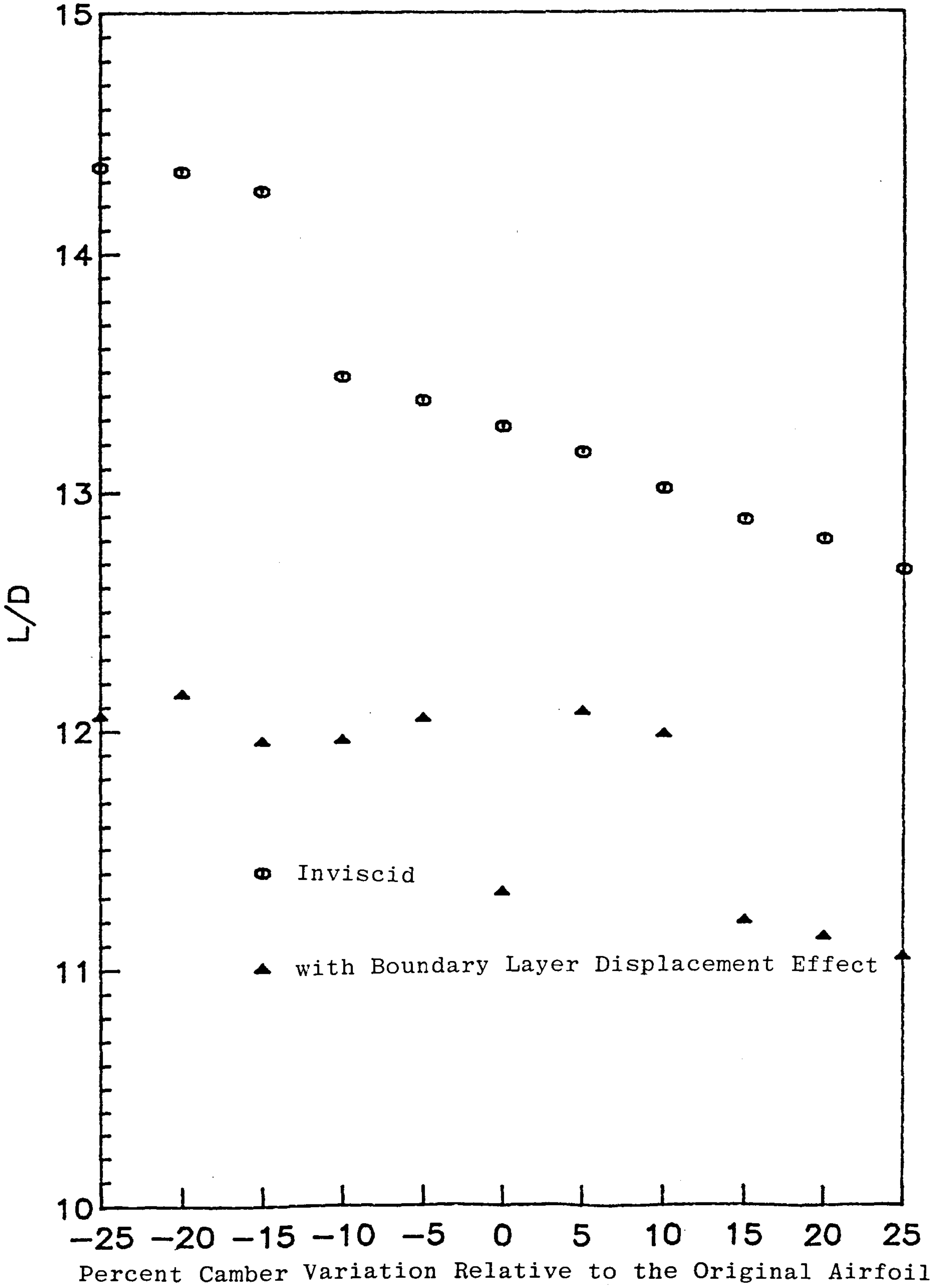

Figure 9d. Camber Effect of a NASA Airfoil on the Lift-Drag Ratios in a Nonuniform Flow at Zero Angle of Attack and Mach Number 0.8

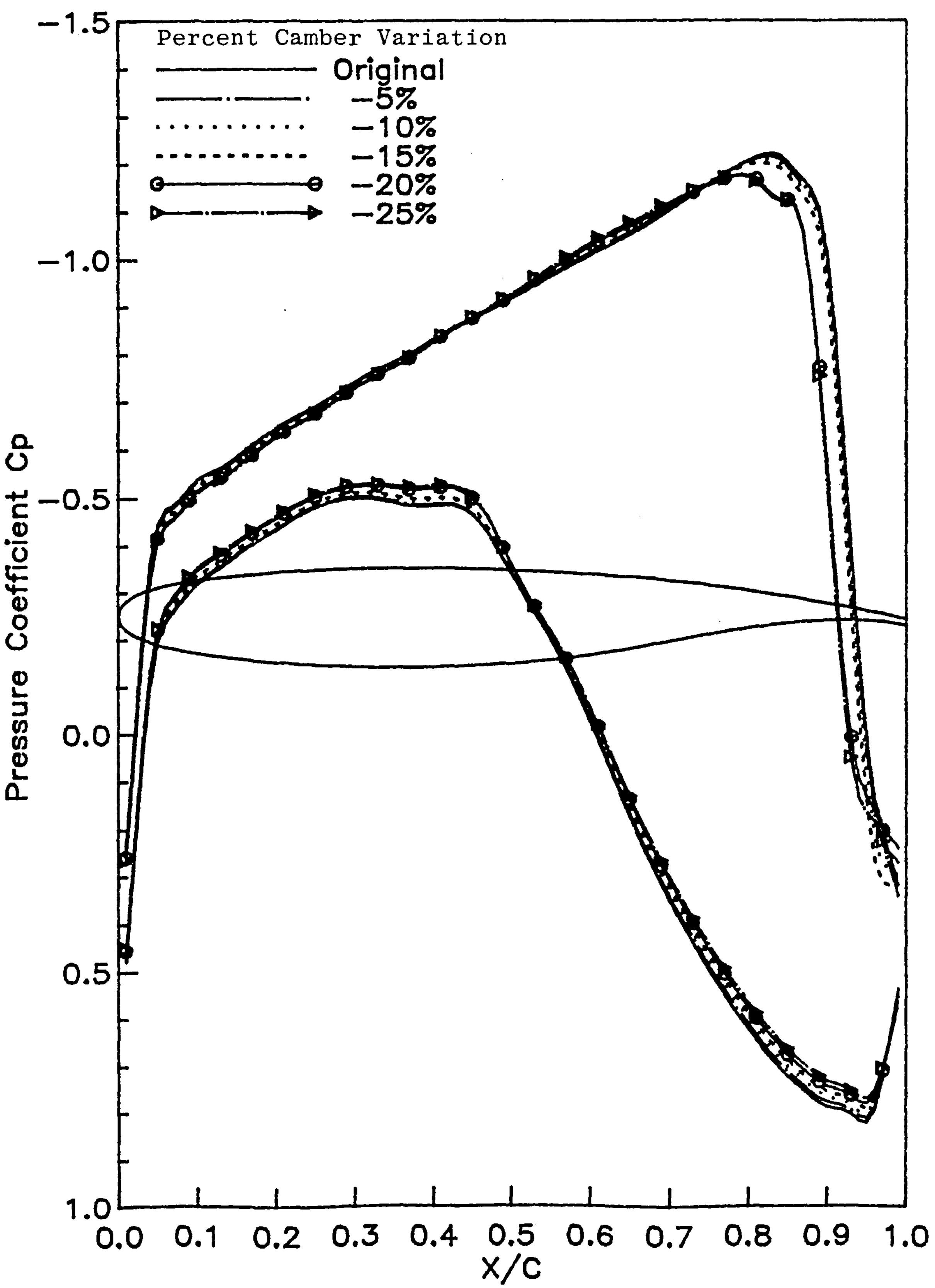

Figure 10a. Camber Effect of a NASA Airfoil on Pressure Distributions in a Nonuniform Flow at Zero Angle of Attack and Mach Number 0.8 Including Boundary Layer Displacement Effect

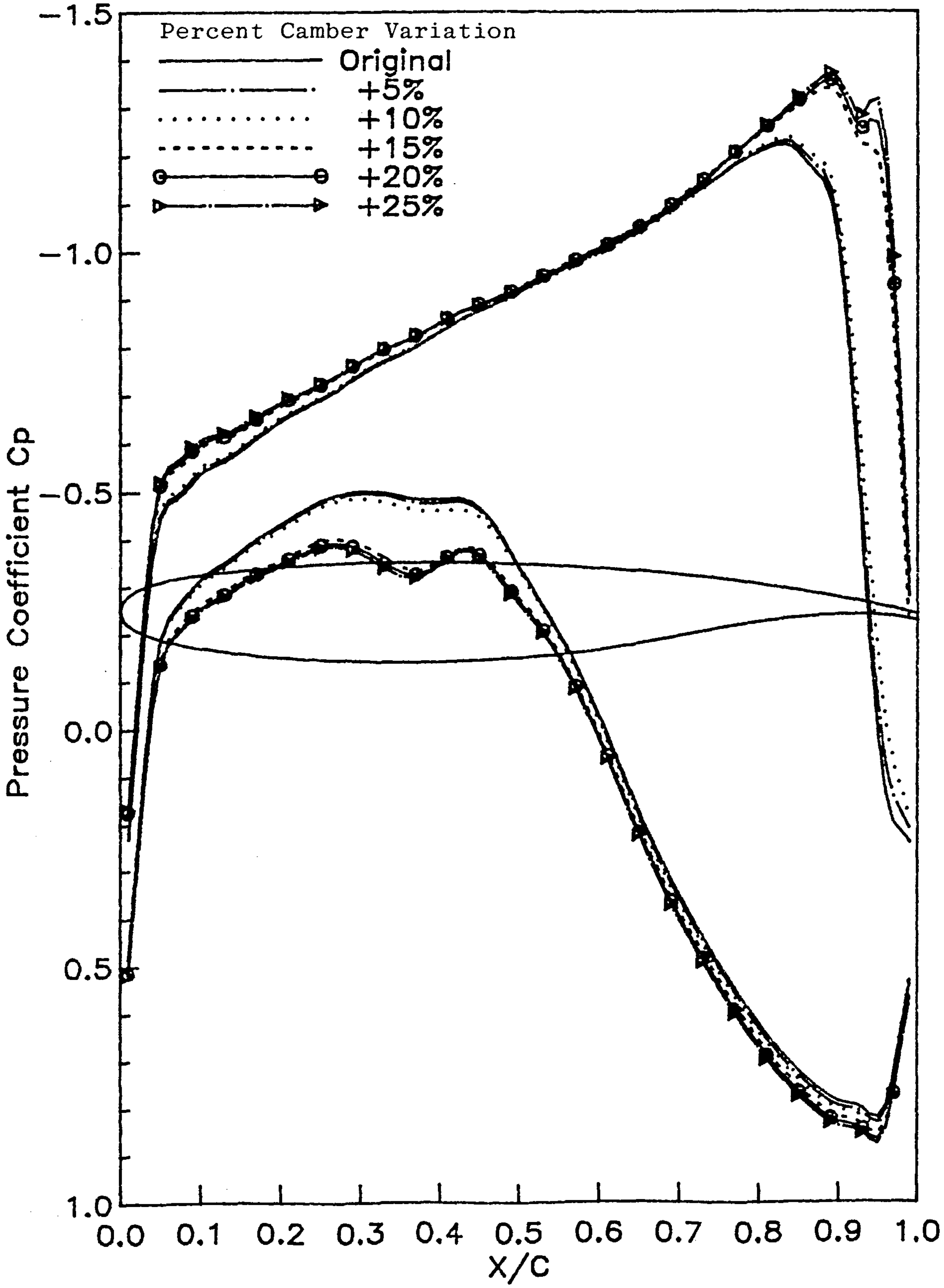

Figure 10b. Camber Effect of a NASA Airfoil on Pressure Distributions in a Nonuniform Flow at Zero Angle of Attack and Mach Number 0.8 Including Boundary Layer Displacement Effect

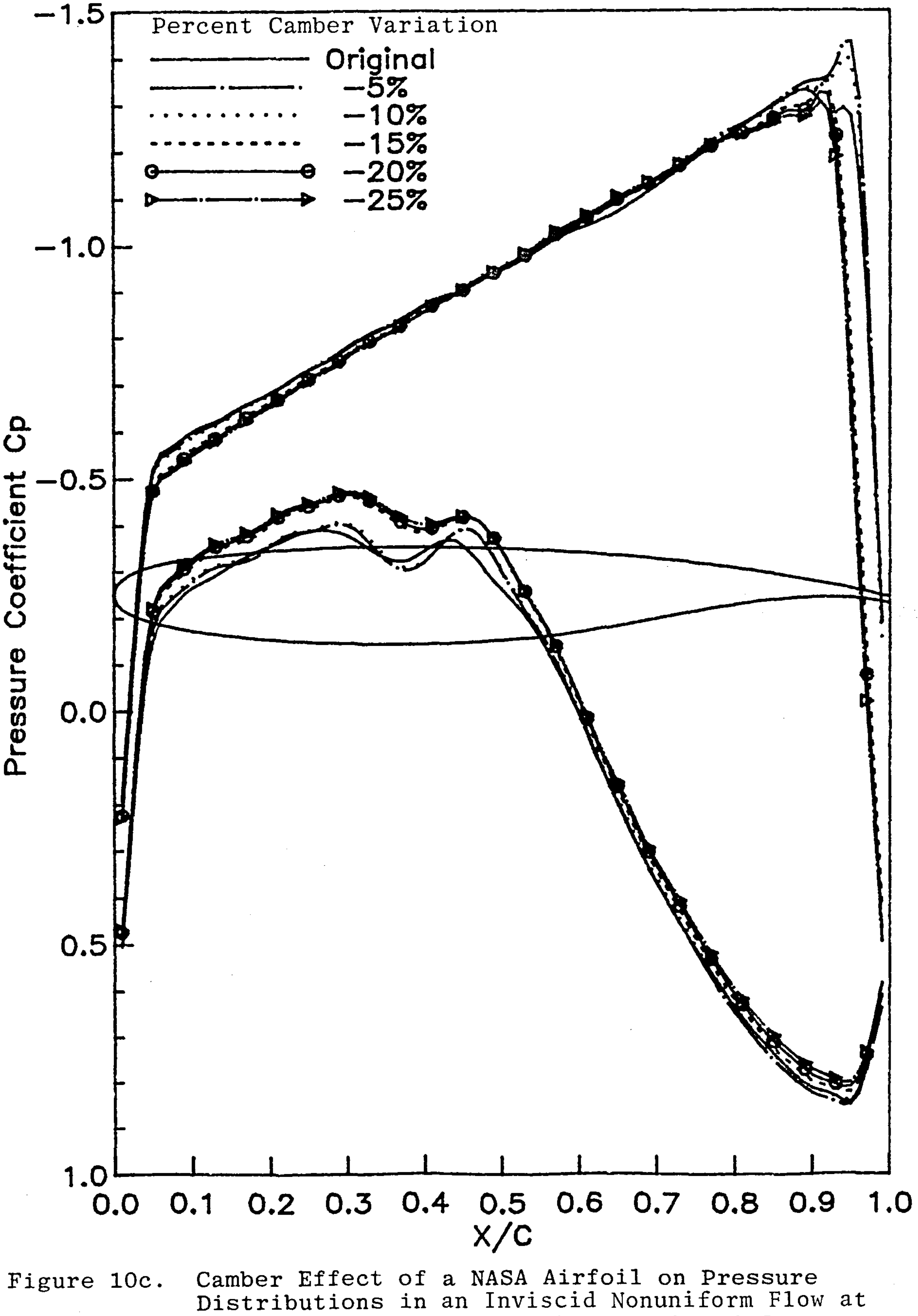

Figure 10c. Camber Effect of a NASA Airfoil on Pressure Distributions in an Inviscid Nonuniform Flow at Zero Angle of Attack and Mach Number 0.8

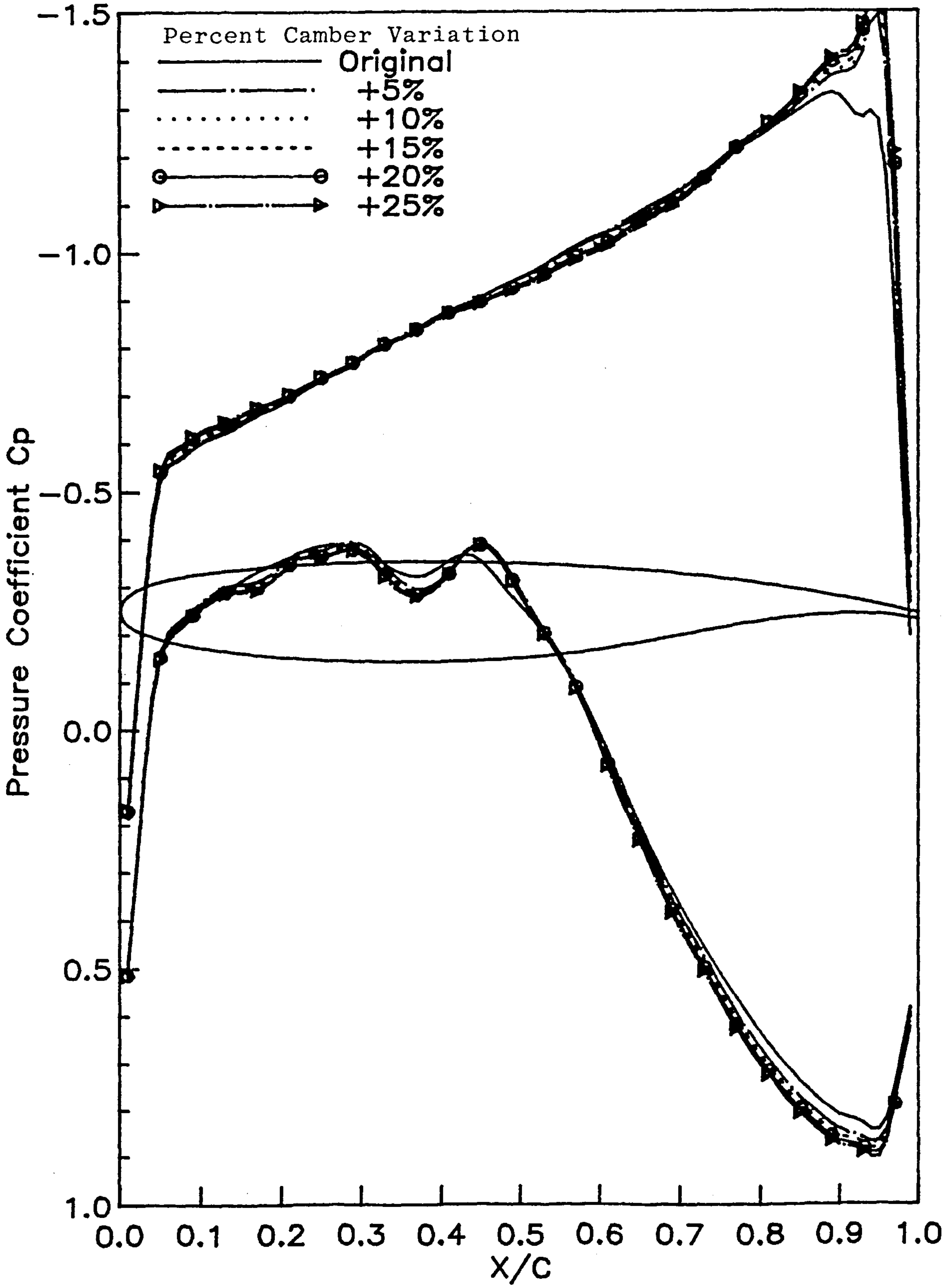

Figure 10d. Camber Effect of a NASA Airfoil on Pressure Distributions in an Inviscid Nonuniform Flow at Zero Angle of Attack and Mach Number 0.8

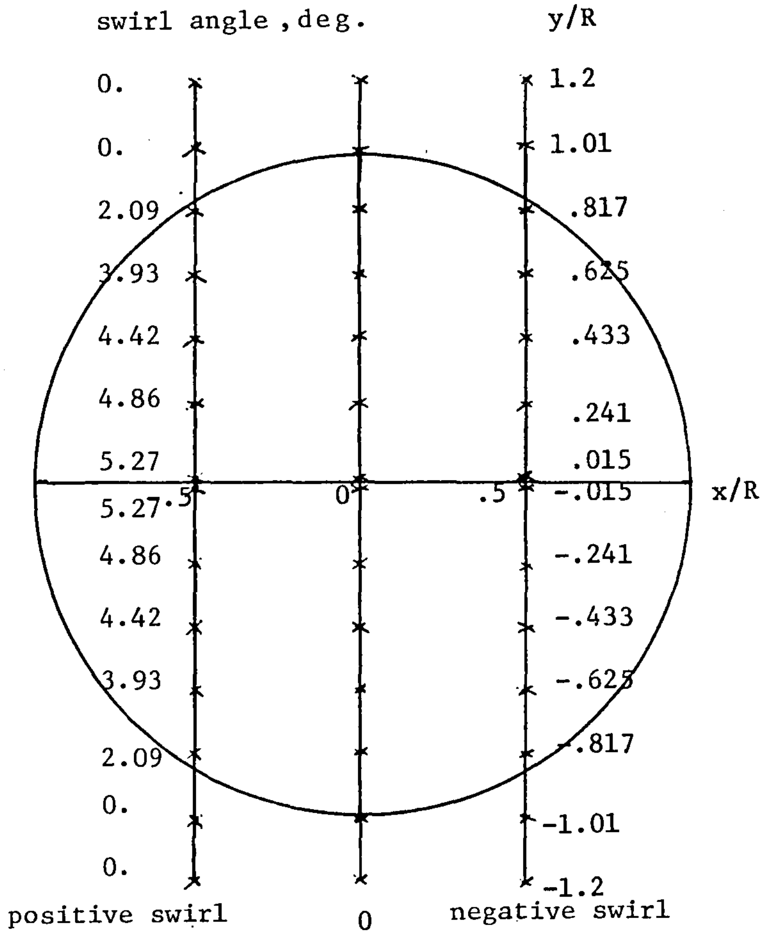

Figure 13. Airfoil Locations Relative to the Propfan Slipstream to Be Examined

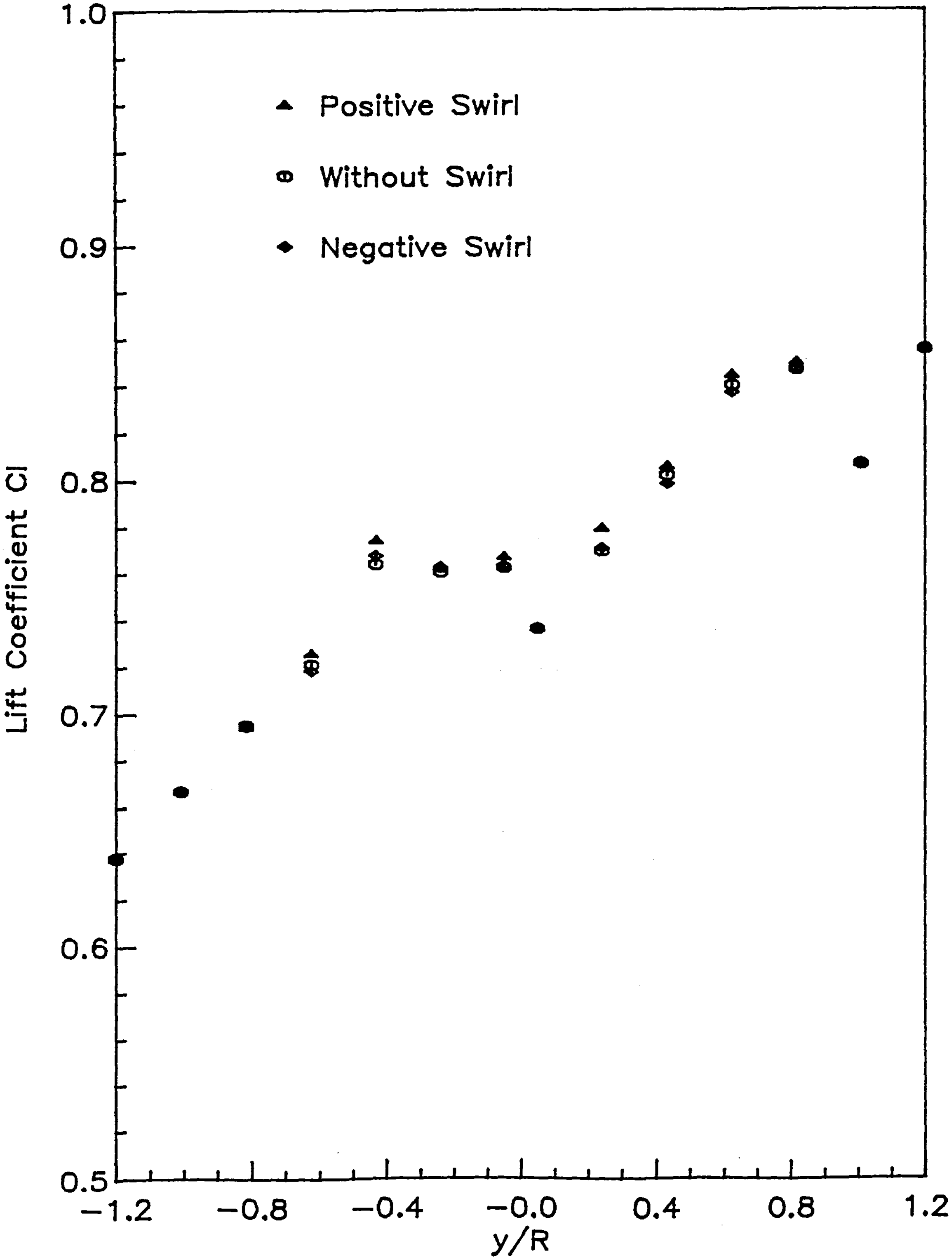

Figure 12a. Lift Coefficient Variations Due to Relative Airfoil-Slipstream Locations in a Nonuniform Flow at Zero Angle of Attack and Mach Number 0.8

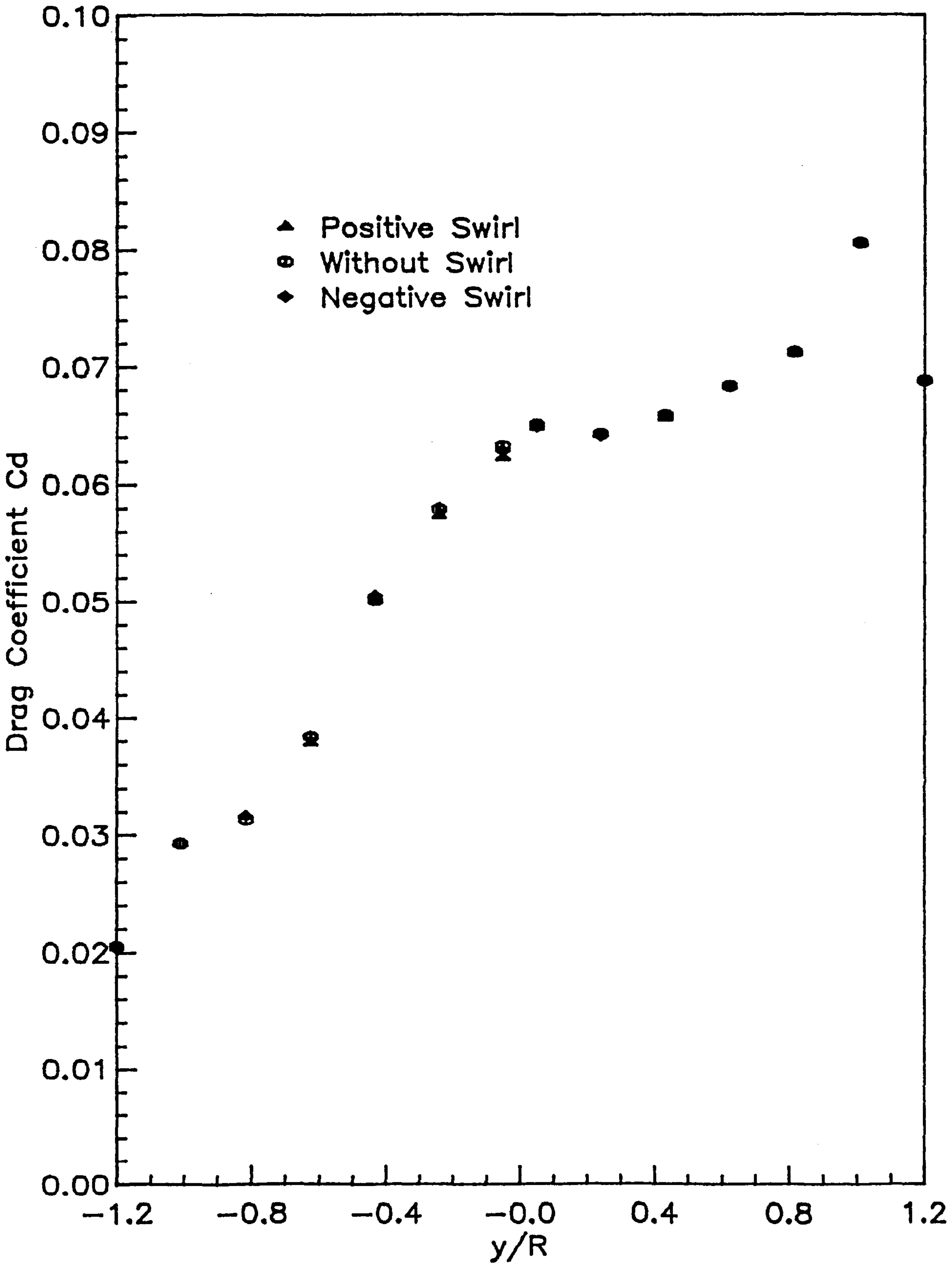

Figure 12b. Drag Coefficient Variations Due to Relative Airfoil-Slipstream Locations in a Nonuniform Flow at Zero Angle of Attack and Mach Number 0.8

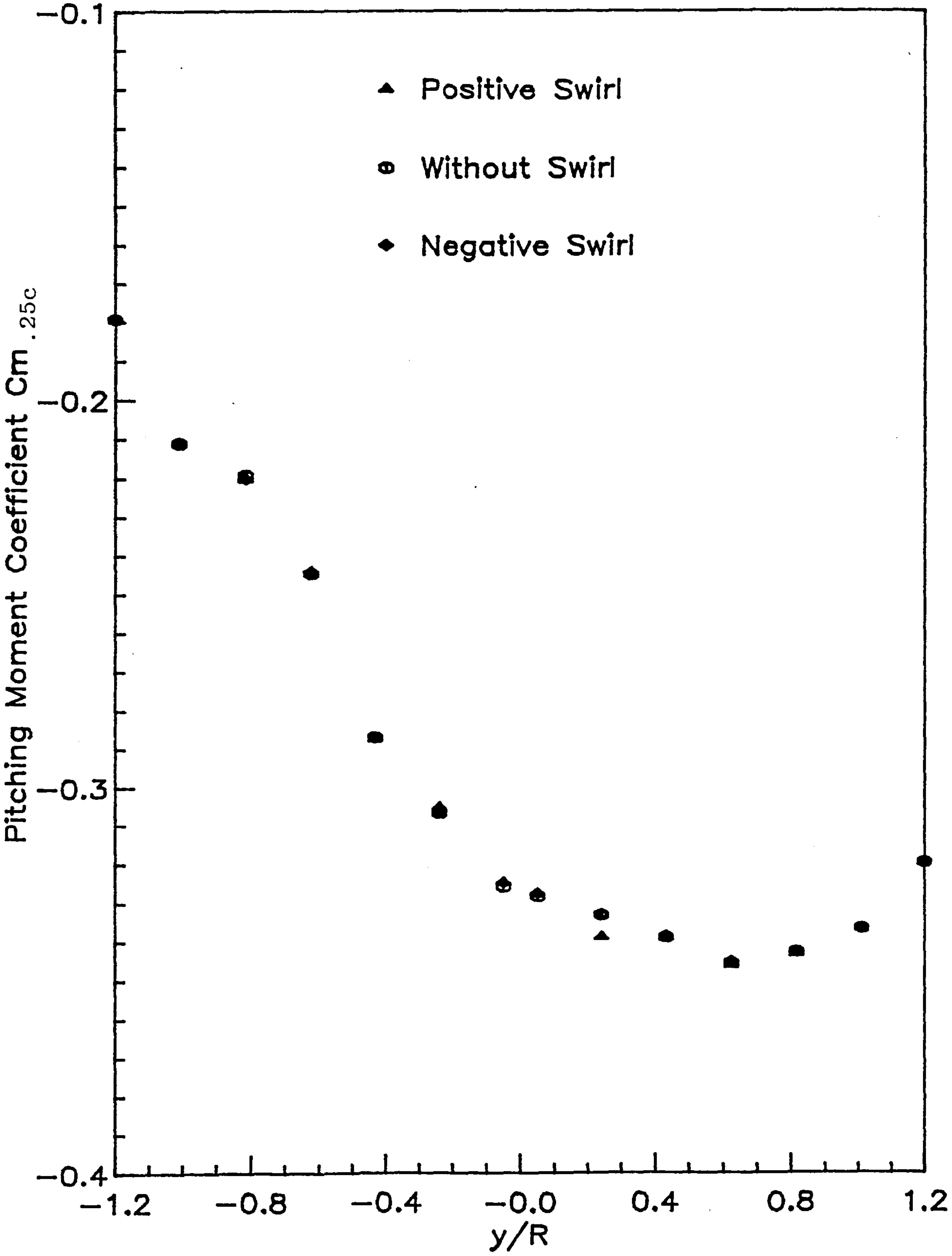

Figure 12c. Pitching Moment Coefficient Variations Due to Relative Airfoil-Slipstream Locations in a Nonuniform Flow at Zero Angle of Attack and Mach Number 0.8

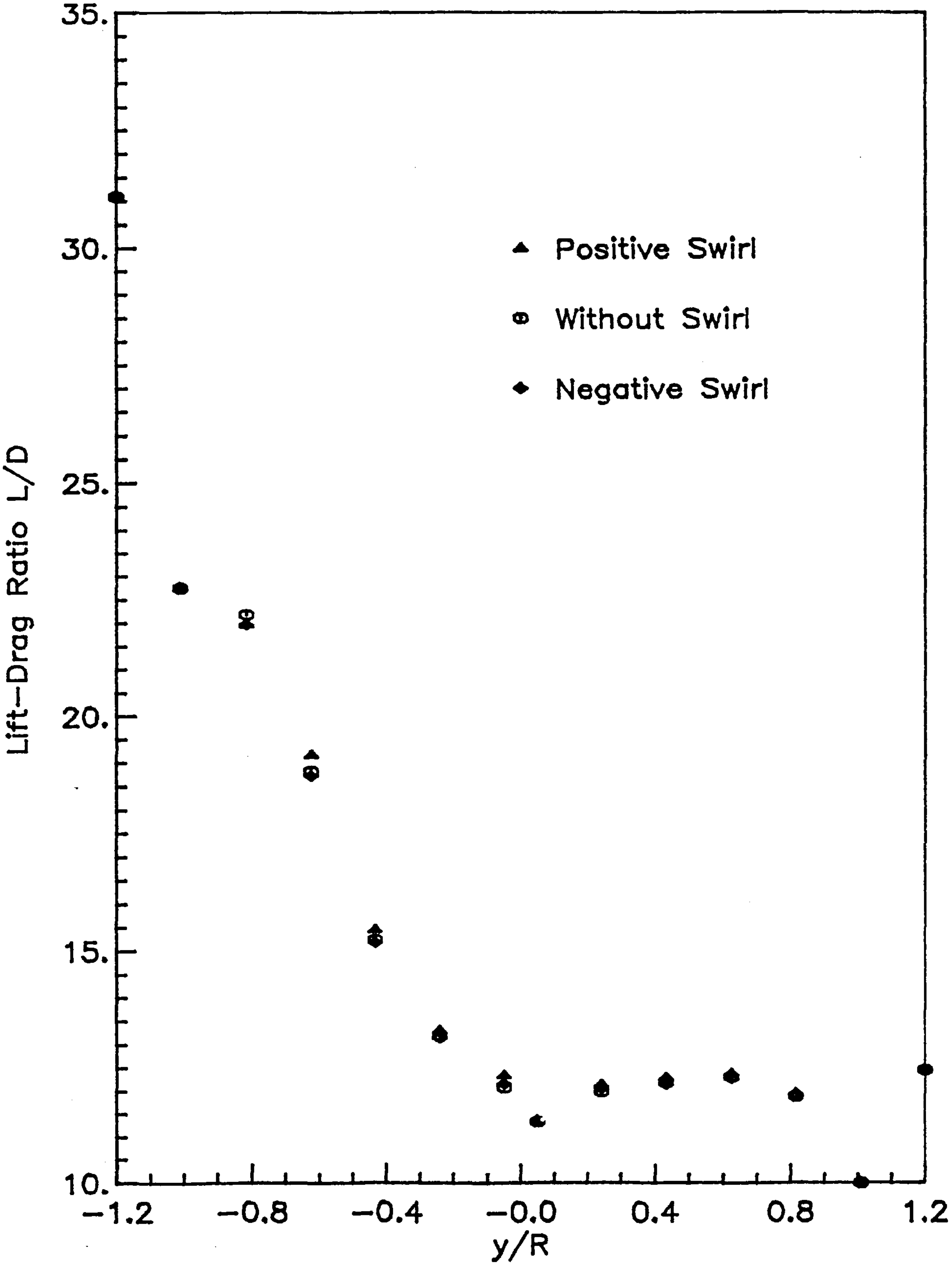

Figure 12d. Lift-Drag Ratio Variations Due to Relative Airfoil-Slipstream Locations in a Nonuniform Flow at Zero Angle of Attack and Mach Number 0.8

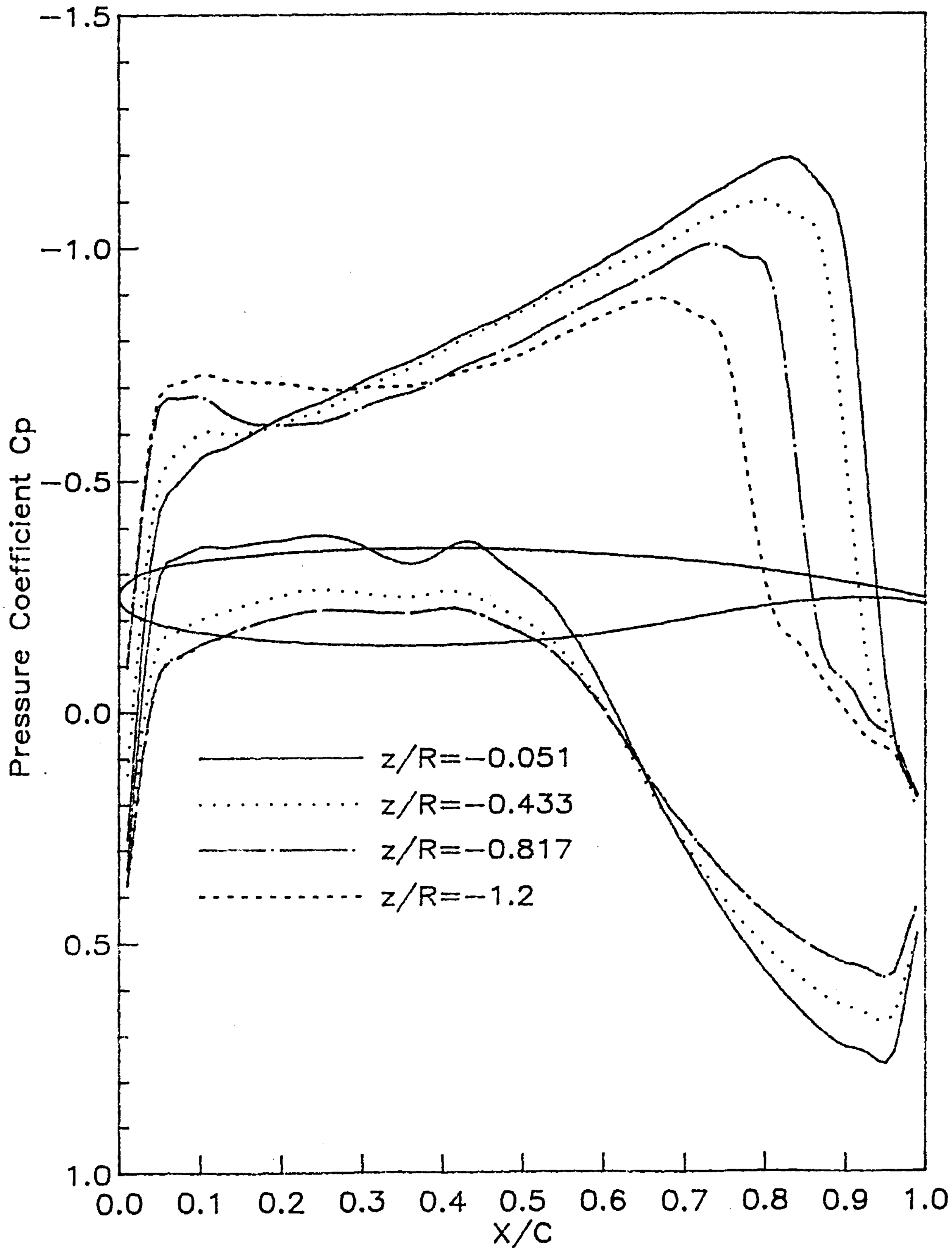

Figure 13a. Pressure Distribution Variations Due to Relative Airfoil-Slipstream Location in a Nonuniform Flow at Zero Angle of Attack and Mach Number 0.8 with Positive Swirl

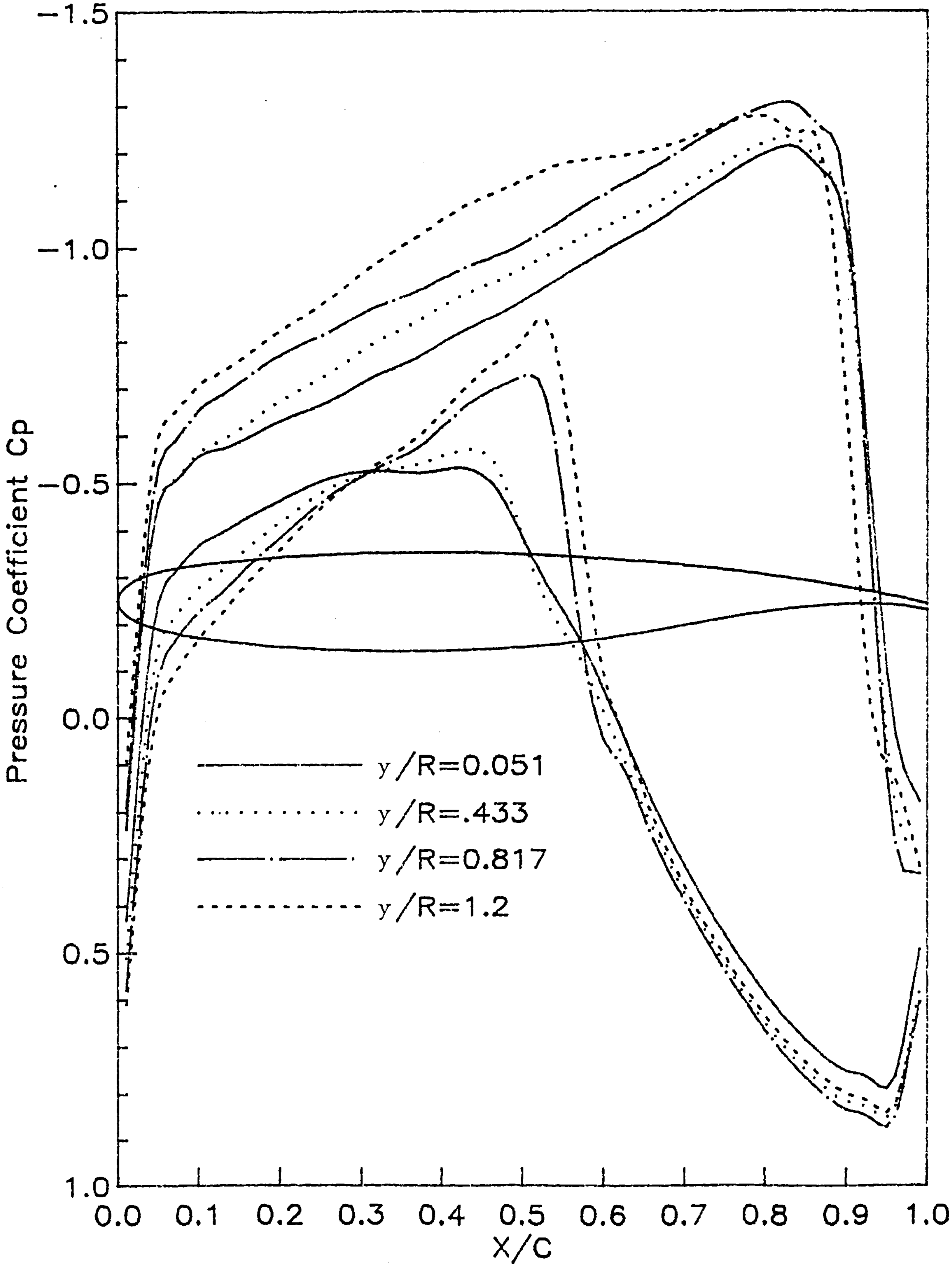

Figure 13b. Pressure Distribution Variations Due to Relative Airfoil-Slipstream Location in a Nonuniform Flow at Zero Angle of Attack and Mach Number 0.8 with Positive Swirl

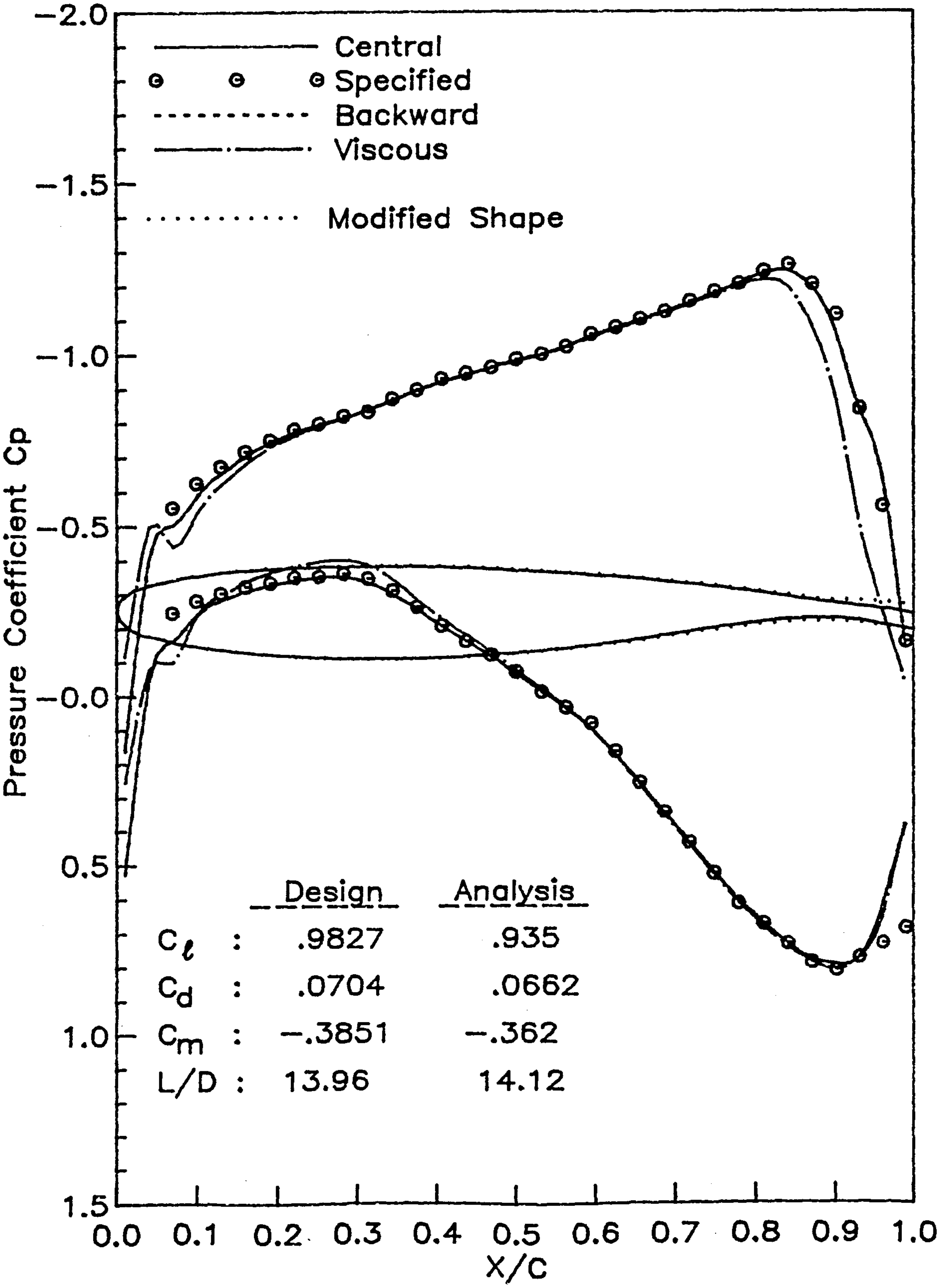

	Design	Analysis
C_ℓ :	.9827	.935
C_d :	.0704	.0662
C_m :	−.3851	−.362
L/D :	13.96	14.12

Figure 14. Comparison of Pressure Terminology for Inverse Airfoil Design in a Nonuniform Flow at Mach Number 0.8

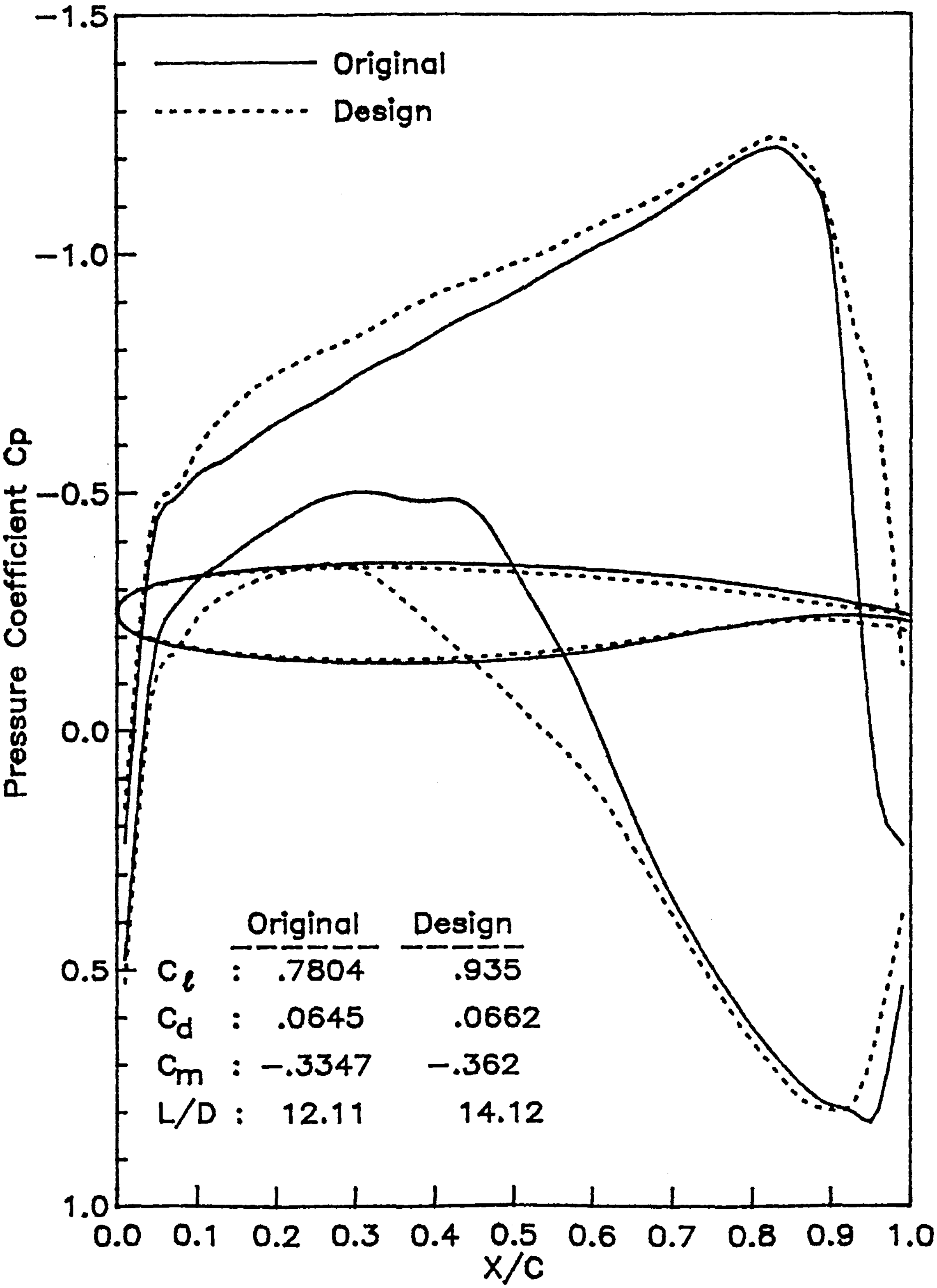

		Original	Design
C_ℓ	:	.7804	.935
C_d	:	.0645	.0662
C_m	:	−.3347	−.362
L/D	:	12.11	14.12

Figure 15. Comparison of Original and Inverse-Design Shapes and Pressure Distributions in a Nonuniform Flow at Mach Number 0.8

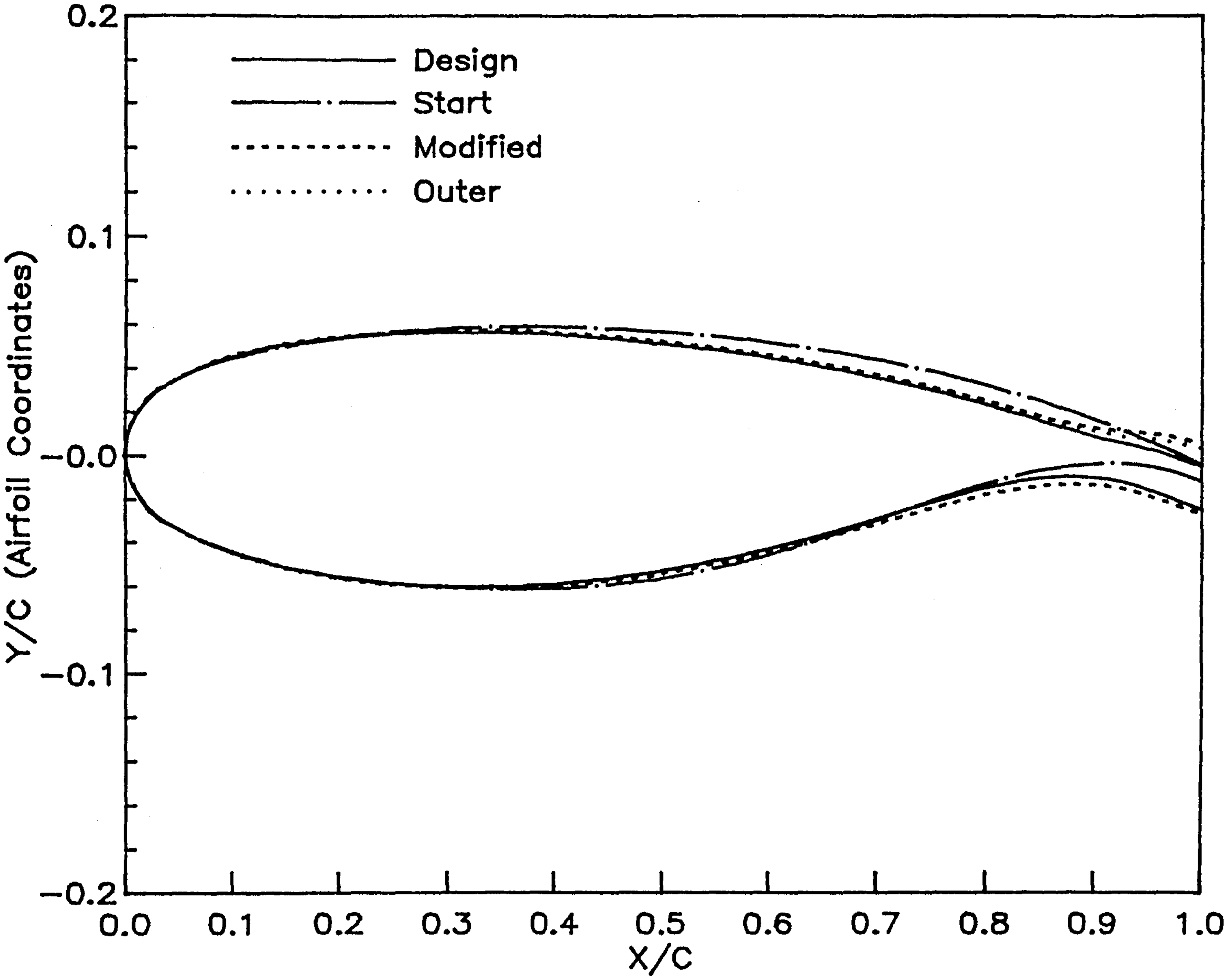

Figure 16. Comparison of Shape Terminology for Inverse Airfoil Design and Original Airfoil in a Nonuniform Flow at Zero Angle of Attack and Mach Number 0.8

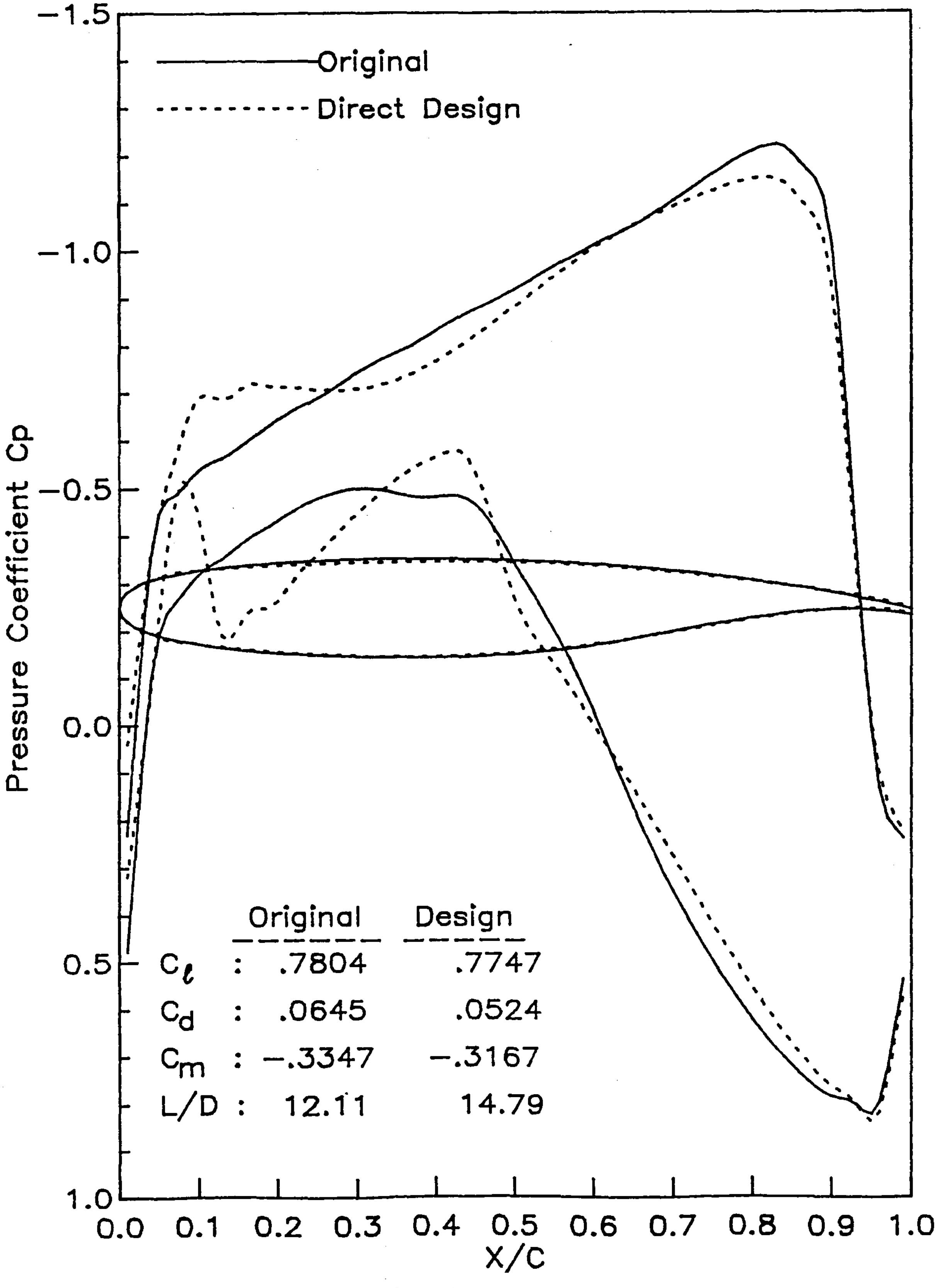

Figure 17. Comparison of Original and Direct-Design Shapes and Pressure Distributions in a Nonuniform Flow at Mach Number 0.8

1. Report No. NASA CR-3991	2. Government Accession No.	3. Recipient's Catalog No.
4. Title and Subtitle Transonic Airfoil Analysis and Design in Nonuniform Flow		5. Report Date June 1986
		6. Performing Organization Code
7. Author(s) Jen-Fu Chang and C. Edward Lan		8. Performing Organization Report No. CRINC-FRL-602-2
9. Performing Organization Name and Address Flight Research Laboratory The University of Kansas Center for Research, Inc. Lawrence, KS 66045		10. Work Unit No.
		11. Contract or Grant No. NAG1-308
12. Sponsoring Agency Name and Address National Aeronautics and Space Administration Washington, DC 20546		13. Type of Report and Period Covered Contractor Report
		14. Sponsoring Agency Code 535-03-01-01
15. Supplementary Notes Langley Technical Monitor: William P. Henderson		

16. Abstract

A nonuniform transonic airfoil code is developed for applications in analysis, inverse design and direct optimization involving an airfoil immersed in propfan slipstream. Problems concerning the numberical stability, convergence, divergence and solution oscillations are discussed. The code is validated by comparing with some known results in incompressible flow. A parametric investigation indicates that the airfoil lift-drag ratio can be increased by decreasing the thickness ratio. A better performance can be achieved if the airfoil is located below the slipstream center. Airfoil characteristics designed by the inverse method and a direct optimization are compared. The airfoil designed with the method of direction optimization exhibits better characteristics and achieves a gain of 22 percent in lift-drag ratio with a reduction of 4 percent in thickness.

17. Key Words (Suggested by Author(s)) Airframe/Propulsion Integration PropFan Transonic Flows	18. Distribution Statement Unclassified-Unlimited Subject Category 02

19. Security Classif. (of this report) Unclassified	20. Security Classif. (of this page) Unclassified	21. No. of Pages 84	22. Price A05

For sale by the National Technical Information Service, Springfield, Virginia 22161

NASA-Langley, 1986

End of Document